

Galactic outflow and diffuse gas properties at $z \geq 1$ using different baryonic feedback models

Paramita Barai,¹★ Pierluigi Monaco,^{1,2} Giuseppe Murante,¹ Antonio Ragagnin² and Matteo Viel^{1,3}

¹INAF – Osservatorio Astronomico di Trieste, Via G.B. Tiepolo 11, I-34143 Trieste, Italy

²Dipartimento di Fisica dell'Università di Trieste, Sezione di Astronomia, Via Tiepolo 11, I-34131 Trieste, Italy

³INFN/National Institute for Nuclear Physics, Via Valerio 2, I-34127 Trieste, Italy

Accepted 2014 November 3. Received 2014 November 1; in original form 2014 September 14

ABSTRACT

We measure and quantify properties of galactic outflows and diffuse gas at $z \geq 1$ in cosmological hydrodynamical simulations. Our novel subresolution model, Multi-Phase Particle Integrator (MUPPI), implements supernova feedback using fully local gas properties, where the wind velocity and mass loading are not given as input. We find the following trends at $z = 2$ by analysing central galaxies having a stellar mass higher than $10^9 M_{\odot}$. The outflow velocity and mass outflow rate (\dot{M}_{out}) exhibit positive correlations with galaxy mass and with the star formation rate (SFR). However, most of the relations present a large scatter. The outflow mass loading factor (η) is between 0.2 and 10. The comparison effective model generates a constant outflow velocity, and a negative correlation of η with halo mass. The number fraction of galaxies where outflow is detected decreases at lower redshifts, but remains more than 80 per cent over $z = 1$ –5. The outflow velocity correlation with SFR becomes flatter at $z = 1$, and η displays a negative correlation with halo mass in massive galaxies. Our study demonstrates that both the MUPPI and effective models produce significant outflows at $\sim 1/10$ of the virial radius; at the same time shows that the properties of outflows generated can be different from the input speed and mass loading in the effective model. Our MUPPI model, *using local properties* of gas in the subresolution recipe, is able to develop galactic outflows whose properties *correlate with global galaxy properties*, and consistent with observations.

Key words: methods: numerical – galaxies: formation – intergalactic medium – cosmology: theory.

1 INTRODUCTION

Baryons existing in cosmic structures regularly undergo the processes of star formation (SF) and supernovae (SN) explosions, which subsequently deposit a fraction of mass/energy to the surroundings. This energy feedback heats up, ionizes, and drives gas outward, often generating large-scale *outflows/winds* (e.g. Burke 1968; Mathews & Baker 1971; Vader 1986; Veilleux, Cecil & Bland-Hawthorn 2005; Rubin et al. 2010). Galactic outflows are observed at low redshifts (e.g. Burbidge, Burbidge & Rubin 1964; Fabbiano & Trinchieri 1984; Ohya, Taniguchi & Terlevich 1997; Smith, Struck & Nowak 2005; Arribas et al. 2014), reaching velocity as large as 1000 km s^{-1} (Diamond-Stanic et al. 2012; Bradshaw et al. 2013), and at high- z (e.g. Frye, Broadhurst & Benitez 2002; Wilman et al. 2005; Weiner et al. 2009; Kornei et al. 2012; Tang

et al. 2014), up to $z \sim 5$ (Dawson et al. 2002), sometimes extending over distances of 60–130 physical kpc (e.g. Steidel et al. 2011; Lundgren et al. 2012).

Winds driven by starbursts and SN are an important source of feedback in galaxy evolution. They are considered to be the primary mechanism by which metals are ejected out of star-forming regions in galaxies and deposited into the circumgalactic medium (CGM) and the intergalactic medium (IGM; e.g. Larson & Dinerstein 1975; Aguirre et al. 2001; Aracil et al. 2004; Fox et al. 2007; Pinsonneault, Martel & Pieri 2010; Gauthier & Chen 2012). They constitute a key ingredient of galaxy formation models, both in hydrodynamic simulations (e.g. Oppenheimer & Davé 2008; Haas et al. 2013; Hirschmann et al. 2013; Bird et al. 2014; Tesfari et al. 2014) and in semi-analytical models (e.g. Baugh 2006; Benson 2012). The outflows are argued to quench SF and suppress the formation of low-mass galaxies, by expelling out gas available to make stars. This in turn flattens the low-mass end of the simulated galaxy mass function (e.g. Theuns et al. 2002; Rasera & Teyssier 2006; Stinson et al.

*E-mail: pbarai@oats.inaf.it

2007), bringing it closer to observations. Feedback is also invoked to reproduce realistic disc galaxies in cosmological hydrodynamic simulations (e.g. Weil, Eke & Efstathiou 1998; Sommer-Larsen, Gotz & Portinari 2003; Okamoto et al. 2005; Scannapieco et al. 2012; Angles-Alcazar et al. 2014).

The physical mechanisms for the origin and driving of galactic winds are complex, occurring on scales of the multiphase structure of the interstellar medium (ISM) and molecular clouds (e.g. Heckman 2003). The gas is likely accelerated either by thermal pressure (e.g. Chevalier & Clegg 1985), radiation pressure (e.g. Murray, Quataert & Thompson 2005) with an impact of dust (Thompson et al. 2014), cosmic rays (e.g. Vazza, Gheller & Bruggen 2014), or a combination of them (e.g. Sharma & Nath 2012). The relevant physical scales are orders of magnitude below the scales resolved in cosmological simulations. Hence energy ejection by starburst and SN are incorporated in the simulations using *subresolution* numerical prescriptions. The physics of the multiphase ISM, on scales unresolved in cosmological simulations, is modelled using spatially averaged properties describing the medium on scales that are resolved.

Thermal feedback, where SN energy is distributed as heating energy of the neighbouring gas, is historically known to be ineffective (e.g. Friedli & Benz 1995; Katz, Weinberg & Hernquist 1996), because fast cooling of the dense SF gas radiates away the thermal energy quickly. A few studies have proposed numerical schemes for efficient thermal feedback in smoothed particle hydrodynamics (SPH) simulations (e.g. Kay, Thomas & Theuns 2003; Dalla Vecchia & Schaye 2012). Depositing the SN energy in the kinetic form is a more popular implementation in the literature, which has been shown to have significant feedback effects (e.g. Navarro & White 1993; Cen & Ostriker 2000; Kawata 2001; Dubois & Teyssier 2008; Oppenheimer et al. 2012). Some other approaches of numerical SN feedback are the following: consider that a part of the neighbouring gas undergoes adiabatic evolution by turning off radiative cooling temporarily (e.g. Mori et al. 1997; Thacker & Couchman 2000; Brook et al. 2005; Stinson et al. 2006; Piontek & Steinmetz 2011); distribute SN energy to hot and cold gas phases separately (e.g. Marri & White 2003; Scannapieco et al. 2006).

Kinetic SN feedback models for cosmological simulations generally impart a velocity kick to the affected gas. An *energy-driven wind* scheme was proposed by Springel & Hernquist (2003), and subsequently used by others (e.g. Tornatore et al. 2004; Dalla Vecchia & Schaye 2008; Tescari et al. 2009; Fabjan et al. 2010; Barai et al. 2013). In this framework, a fraction of SN energy provides the outflow kinetic energy, and the wind speed is constant. Other models formulate the outflow velocity and mass loading factor in terms of galaxy global properties [mass, velocity dispersion, star formation rate (SFR)]: *momentum-driven wind* (e.g. Oppenheimer & Davé 2008; Tescari et al. 2009), dependent on the local velocity dispersion of the dark matter (DM; Okamoto et al. 2010); multicomponent and variable velocity galactic outflow (Choi & Nagamine 2011); halo-mass-dependent energy-driven outflow (Puchwein & Springel 2013); and combination of both energy-driven and momentum-driven cases (Schaye et al. 2010). Very recently Schaye et al. (2015) presented results from a stochastic implementation of thermal SN feedback, where galactic winds develop without imposing any input outflow velocity and mass loading factor.

In our current work we explore the novel subresolution model Multi-Phase Particle Integrator (MUPPI, Section 2.4; Murante et al. 2010, 2015). It consists of a scheme of SF in multiphase ISM, where the system of ordinary differential equations is numerically integrated within the hydrodynamical time step. MUPPI incorporates

a direct distribution of thermal and kinetic energy from SN to the neighbouring gas, using local properties of the gas, and the free parameters of feedback energy efficiency fraction and a probability. Thus our model has no input expression of wind velocity and mass loading for SN feedback. Additionally our formulation, unlike widely done in the literature, has no dependence on global properties like galaxy mass or velocity dispersion. The MUPPI model has been shown to reproduce the Schmidt–Kennicutt relation (Monaco et al. 2012), predicts a warm mode of gas accretion on forming galaxies (Murante et al. 2012), generates realistic disc galaxies at a moderate resolution (Murante et al. 2015), and the properties of bars in spiral galaxies were studied (Goz et al. 2014). For comparison with MUPPI, we adopt the effective SF model (Springel & Hernquist 2003) with two variations of energy-driven wind: a constant velocity, and where the wind velocity depends on distance from galaxy centre (Barai et al. 2013) following a correlation motivated by the observational studies of Steidel et al. (2010).

Studies have analysed CGM gas inflows and outflows in cosmological hydrodynamic simulations. Oppenheimer & Davé (2008) tracked wind particles (Section 2.3) and computed the feedback mass and energy outflow rate as a function of galaxy baryonic mass. Oppenheimer et al. (2010) followed the gas previously ejected in winds and accreting for new SF at $z < 1$, measuring the recycling time. Ford et al. (2013) investigated the CGM dynamical state by tracking inflowing, outflowing, and ambient gas based on cross-correlation of the gas particle locations between $z = 0.25$ and 0 with respect to galaxy positions. van de Voort & Schaye (2012) presented gas physical property (density, temperature) radial profiles, for all, inflowing and outflowing gas, inside and around galaxy haloes at $z = 2$. Using a different set of numerical schemes in the zoom-in simulation of a massive galaxy at $z = 3$, Shen et al. (2012) presented the time evolution of outflow velocity, metallicity, and the mass-loading factor for the main host and the massive dwarf galaxies. In similar zoom simulations, Brook et al. (2013) examined the time evolution of gas outflow rates through $R_{\text{vir}}/8$, and their metallicities. Performing 3D hydrodynamic simulations of a disc–halo system on 10s-pc scale, von Glasow et al. (2013) injected SN energy as superbubbles, and studied the development of bipolar outflows, together with their mass and energy loss rates.

In this paper we perform a quantification of SN-driven galactic outflow properties in cosmological hydrodynamical simulations. As described earlier, outflows as widely observed in galaxies are generated in simulations using thermal or (more popularly) kinetic SN feedback. In several cases a pre-defined wind velocity and mass loading factor are input to the subresolution model. However the velocity and mass loading which are imparted to the gas in a numerical scheme might not be the speed and rate with which an outflow actually develops. This is because the outflow propagates through the atmosphere of a galaxy and interacts with surrounding gas. Therefore determining these properties explicitly is necessary for a complete study of simulated galactic outflows, which we do in this paper. Furthermore, the MUPPI model has no input expression of wind velocity and mass loading for SN feedback. We compute the velocity, mass outflow rate, and mass loading of our simulated galaxies, and investigate how differently MUPPI drives outflows than other models. We measure the characteristics of outflows of a statistical sample of galaxies extracted from cosmological simulations, over redshifts $z = 1$ –5, aiming to infer possible correlations with galaxy mass and SFR. We also study the properties of diffuse gas in the CGM of galaxies.

This paper is organized as follows: we describe our numerical code in Section 2, the simulations in Section 3, present and discuss

Table 1. Simulation parameters. Column (1): name of simulation run. Column (2): L_{box} = comoving side of cubic simulation volume. Column (3): total number of gas and DM particles in the initial condition. Column (4): mass of gas particle (which has not undergone any star formation). Column (5): mass of star particle. Column (6): gravitational softening length (of all particle types). Column (7): model of SF and SN feedback. Column (8): v_w = wind velocity. Column (9): $f_{\text{fb, out}}$ = thermal feedback energy fraction. Column (10): $f_{\text{fb, kin}}$ = kinetic feedback energy fraction. Column (11): P_{kin} = probability of kicking gas particles into wind.

Run name	L_{box} (Mpc)	N_{part} (3)	m_{gas} (M_{\odot}) (4)	m_{\star} (M_{\odot}) (5)	L_{soft} (kpc) (6)	SF and SN feedback subresolution physics model (7)	v_w (8)	$f_{\text{fb, out}}$ (9)	$f_{\text{fb, kin}}$ (10)	P_{kin} (11)
<i>E35nw</i>	35.56	2×320^3	8.72×10^6	2.18×10^6	2.77 (comoving)	Effective	0			
<i>E35rvw</i>	35.56	2×320^3	8.72×10^6	2.18×10^6	2.77 (comoving)	Effective	$v_w(r)$			
<i>E25cw</i>	25	2×256^3	5.36×10^6	1.34×10^6	0.69 (physical)	Effective	350			
<i>M25std</i>	25	2×256^3	5.36×10^6	1.34×10^6	0.69 (physical)	MUPPI		0.2	0.6	0.03
<i>M25a</i>	25	2×256^3	5.36×10^6	1.34×10^6	0.69 (physical)	MUPPI		0.4	0.4	0.03
<i>M25b</i>	25	2×256^3	5.36×10^6	1.34×10^6	0.69 (physical)	MUPPI		0.2	0.8	0.03
<i>M25c</i>	25	2×256^3	5.36×10^6	1.34×10^6	0.69 (physical)	MUPPI		0.2	0.6	0.01
<i>M25d</i>	25	2×256^3	5.36×10^6	1.34×10^6	0.69 (physical)	MUPPI		0.2	0.6	0.06
<i>M50std</i>	50	2×512^3	5.36×10^6	1.34×10^6	0.69 (physical)	MUPPI		0.2	0.5	0.03

our results in Section 4, and finally give a summary of the main findings in Section 5.

2 NUMERICAL METHOD

We use a modified version of the TreePM (particle mesh)–smoothed particle hydrodynamics (SPH) code GADGET-3, which includes a more efficient domain decomposition to improve the work-load balance over GADGET-2 (Springel 2005). The additional subresolution¹ physics included in our code are outlined below. There is no active galactic nuclei (AGN) feedback in our models.

2.1 Radiative cooling

Radiative cooling is implemented by adopting the cooling rates from the tables of Wiersma, Schaye & Smith (2009), which includes metal-line cooling. 11 element species (H, He, C, Ca, O, N, Ne, Mg, S, Si, Fe) are tracked for constructing the cooling tables. Heating from a spatially uniform time-dependent photoionizing radiation is considered from the cosmic microwave background and the Haardt & Madau (2001) model for the ultraviolet (UV)/X-ray background produced by quasars and galaxies. The gas is assumed to be dust-free, optically thin, and in (photo)ionization equilibrium. Contributions from the 11 elements are interpolated as a function of density, temperature, and redshift from tables that have been pre-computed using the public photoionization code CLOUDY (last described by Ferland et al. 1998). Note that one simulation (*M50std*, defined in Table 1) is done using cooling rates from the tables of Sutherland & Dopita (1993), which tracks eight elements (H, He, C, O, Mg, S, Si, Fe). In this case, the relative abundance of various metals in gas is fixed to solar, and only the overall metallicity counts to computing the cooling rates.

2.2 Chemical evolution

Stellar evolution and chemical enrichment are followed according to the model introduced by Tornatore et al. (2007). Each star particle is treated as a simple stellar population (SSP). Given a stellar initial mass function (IMF), the mass of the SSP is varied in time following

¹ *Subresolution* refers to processes occurring at physical scales smaller than the resolved scales in our simulations.

the death of stars, and accounting for stellar mass losses. Production of nine metal species (C, Ca, O, N, Ne, Mg, S, Si, Fe) is accounted for using yields from Type Ia SN (SN-Ia; Thielemann et al. 2003), Type II SN (SN-II; Woosley & Weaver 1995), as well as asymptotic giant branch stars (van den Hoek & Groenewegen 1997). Different stellar populations release metals with mass-dependent time delays, where the lifetime function by Padovani & Matteucci (1993) is adopted. The mass range for SN-II is $M/M_{\odot} > 8$, while that for SN-Ia originating from binary systems is $0.8 < M/M_{\odot} < 8$ with a binary fraction of 10 per cent. SN-Ia (present only in the effective model – Section 2.3, not in MUPPI – Section 2.4) and SN-II contribute to thermal energy feedback.

The seven new simulations presented in this paper (Section 3) assume a fixed stellar IMF following Kroupa, Tout & Gilmore (1993), in the mass range (0.1–100) M_{\odot} . Two older simulations (used for comparison) include an IMF by Chabrier (2003). The two IMFs are similar in the mass range considered, so we assume they do not cause any difference in our outflow analysis results. Stars within a mass interval [8–40] M_{\odot} become SN first before turning into black holes (BHs) at the end of their lives, while stars of mass $>40 M_{\odot}$ are allowed to directly end in BHs without contributing to enrichment. Here by BH we mean stellar mass BHs, whose evolution is not followed; they enter only in the stellar evolution prescriptions.

The chemical evolution model also incorporates mass loss through stellar winds and SN explosions, which are self-consistently computed for a given IMF and lifetime function. A fraction of a star particle’s mass is restored as diffuse gas during its evolution, and distributed to the surrounding gas. The enriched material is spread among the neighbouring gas particles with weights given by the SPH kernel.

2.3 Effective model of SF and SN feedback

In this model, SF follows the effective subresolution scheme by Springel & Hernquist (2003). Gas particles with density above a limiting threshold, $n_{\text{SF}} = 0.13 \text{ cm}^{-3}$ (in units of number density of hydrogen atoms), are considered to contain two phases: cold condensed clouds, and ambient hot gas, in pressure equilibrium. Each gas particle represents a region of the ISM, where the cold clouds supply the material available for SF. The star-forming gas remains in self-regulated equilibrium. Star particles are collisionless, and are spawned from gas particles undergoing SF, according to the

stochastic scheme introduced by Katz et al. (1996). We allow a gas particle to spawn up to four generations of star particles.

Kinetic feedback from SN is included following the *energy-driven* outflow prescription (originally from Springel & Hernquist 2003). The wind mass-loss rate (\dot{M}_w) relates to the SF rate (\dot{M}_*) via the mass loading factor (η),

$$\dot{M}_w = \eta \dot{M}_*. \quad (1)$$

Observations reveal that mass outflow rates in galaxies are comparable to or a few times larger than their SF rates (e.g. Martin 1999; Pettini et al. 2002; Bouche et al. 2012; Newman et al. 2012). Thus, following Springel & Hernquist (2003), we adopt a constant $\eta = 2$.

The wind kinetic energy is a fixed fraction χ of SN energy:

$$\frac{1}{2} \dot{M}_w v_w^2 = \chi \epsilon_{\text{SN}} \dot{M}_*. \quad (2)$$

Here v_w is the wind velocity, ϵ_{SN} is the average energy released by SN for each M_\odot of stars formed under the instantaneous recycling approximation. Combining equations (1) and (2), v_w can be rewritten as

$$v_w = \left(\frac{2\chi\epsilon_{\text{SN}}}{\eta} \right)^{1/2}. \quad (3)$$

Following a series of studies (e.g. Tornatore et al. 2007; Tescari et al. 2011; Barai et al. 2013), and unlike Springel & Hernquist (2003), we choose v_w as a free parameter. For our adopted Chabrier power-law IMF (Section 2.2), $\epsilon_{\text{SN}} = 1.1 \times 10^{49}$ erg M_\odot^{-1} .

We explore two different outflow models: constant v_w and radially varying v_w . In the latter, developed in Barai et al. (2013), the wind velocity depends on galactocentric radius (r , or distance from galaxy centre), following a correlation motivated by the observational studies of Steidel et al. (2010):

$$v_w(r) = v_{\text{max}} \left(\frac{r_{\text{min}}^{1-\alpha} - r^{1-\alpha}}{r_{\text{min}}^{1-\alpha} - R_{\text{eff}}^{1-\alpha}} \right)^{0.5}. \quad (4)$$

Here r_{min} is the distance from which the wind is launched and where the velocity is zero, R_{eff} represents the outer edge of gas distribution, v_{max} is the velocity at R_{eff} , and α is a power-law index. We choose the following parameters for our simulation run *E35rvw* (Section 3): $r_{\text{min}} = 1 h^{-1}$ kpc, $R_{\text{eff}} = 100 h^{-1}$ kpc, $v_{\text{max}} = 800$ km s^{-1} , and $\alpha = 1.15$.

2.4 MUPPI model of SF and SN feedback

The original MUPPI subresolution algorithm is described in Murante et al. (2010), and its latest features (chemical evolution, metal cooling, SN kinetic feedback) in Murante et al. (2015). Gas particles undergoing SF are assumed (following Monaco 2004, originally from Springel & Hernquist 2003) to represent a multiphase ISM composed of hot and cold phases, in pressure equilibrium. A fraction of the cold phase (the molecular gas fraction) provides the reservoir for SF. Star particles are created by a stochastic algorithm (as in Section 2.3). The hot phase is heated by the energy from massive and dying stars and radiatively cools.

A gas particle enters the multiphase regime whenever its temperature drops below 10^5 K, and its density is higher than a threshold ρ_{thr} (not to be confused with the SF density threshold n_{SF} in Section 2.3). A multiphase particle's evolution is governed by four ordinary differential equations (ODEs) in terms of masses of three (hot, cold, stellar) components and thermal energy of the hot phase. Matter flows among the three components: cooling deposits hot gas into the cold phase; evaporation brings cold gas back to the hot

phase; SF moves mass from the cold gas to stars; restoration moves mass from stars back to the hot phase. Within each SPH time step, the ODEs are integrated using a Runge–Kutta method with adaptive time steps, making the integration time step much shorter than the SPH one. A multiphase cycle can last up to time t_{clock} , set proportional to the dynamical time of the cold phase. A gas particle is no longer multiphase when its density reaches below $\rho_{\text{th}}/5$. Moreover, at low densities if SN energy is not sufficient to sustain a hot phase (rendering a hot temperature below 10^5 K), the particle is forced to exit the multiphase regime. Opposed to the effective model, no equilibrium hypothesis is imposed in MUPPI. Here properties of the ISM interact with the varying hydrodynamical properties obtained from the gas evolution.

Energy from SN is distributed in both thermal and kinetic forms. The total thermal energy ejected by each star-forming multiphase particle is

$$\Delta E_{\text{heat,o}} = E_{\text{SN}} f_{\text{fb,out}} \frac{\Delta M_*}{M_{*,\text{SN}}}. \quad (5)$$

Here E_{SN} is the energy of a single SN, and $M_{*,\text{SN}}$ the stellar mass associated with each SN event. The thermal energy is deposited to gas neighbours within the particle's SPH smoothing length, and lying inside a cone of axis along the direction of minus the local density gradient and having a semi-aperture angle $\theta = 60^\circ$. This mimics the blowout of superbubbles along the path of least resistance (see Monaco 2004). Energy contributions are weighted by the SPH kernel, using the distance from the cone axis. This thermal feedback scheme is relatively effective even at high densities.

For kinetic SN feedback, when a gas particle exits a multiphase cycle, a probability P_{kin} to become a 'wind particle' is assigned to it. The wind particles can receive kinetic energy from neighbouring multiphase particles for a time t_{wind} . Assuming that outflows are driven by SN-II exploding from molecular cloud destruction, this time is set equal to the lifetime of an $8 M_\odot$ star, t_8 , minus the duration t_{clock} of the past multiphase cycle:

$$t_{\text{wind}} = t_8 - t_{\text{clock}}. \quad (6)$$

The wind phase quits earlier than t_{wind} whenever the wind (gas) particle falls to a density below $0.3\rho_{\text{thr}}$. For each star-forming particle, the available kinetic energy is

$$E_{\text{kin}} = f_{\text{fb,kin}} E_{\text{SN}}. \quad (7)$$

The kinetic energy is distributed (using the same scheme as thermal energy) to wind particles inside the SPH kernel of the multiphase particle and within a cone of semi-aperture θ antialigned with the density gradient, and the energy contribution is weighted by the distance from the cone axis. The eligible wind particles receive 'velocity kicks' as follows. For each wind particle, the energy contribution from all kicking particles is computed, and the energy-weighted average vector from kicking particles to the wind one. Then the kinetic energy of the wind particle is increased,² with the velocity increase in the direction defined above. In order to avoid hydrodynamical coupling at \sim kpc scale, a wind particle is decoupled from its surrounding gas as long as it remains in the wind phase.

The free parameters of the SN feedback prescription are $f_{\text{fb,out}}$, $f_{\text{fb,kin}}$, and P_{kin} ; the values we explore are given in Table 1 and Section 3. At variance with other kinetic wind models in the literature, neither the outflow velocity nor the mass-loading is given as input quantities. Nevertheless, typical values of these can be estimated

² In the reference frame of the particle itself.

theoretically (Murante et al. 2015). With the default parameters, the mass load factor estimate is

$$\langle \eta \rangle = \frac{\dot{M}_{\text{wind}}}{\dot{M}_{\text{sfr}}} = \frac{P_{\text{kin}}}{\langle f_{\text{cold}} \rangle \langle f_{\text{mol}} \rangle f_*} \simeq 1.5, \quad (8)$$

and the mass-weighted average wind velocity:

$$\langle v_{\text{wind}} \rangle = \sqrt{\frac{f_{\text{fb,kin}} E_{\text{SN}}}{\langle \eta \rangle \langle M_{*,\text{SN}} \rangle}} \simeq 600 \text{ km s}^{-1}, \quad (9)$$

where $\langle \rangle$ indicates that average values for star-forming ISM are used. Furthermore, the MUPPI feedback implementation uses only local properties of the gas.

3 SIMULATIONS

Our series of simulations is listed in Table 1. Cosmological volumes are evolved, with periodic boundary conditions, starting from an equal number of DM and gas particles at $z = 99$, up to $z = 0$. The initial conditions have been generated using the CAMB³ software (Lewis, Challinor & Lasenby 2000). A concordance flat Λ cold dark matter (Λ CDM) model is used, in agreement with recent observations of the cosmic microwave background radiation, weak gravitational lensing, Lyman α forest, and galaxy cluster mass function evolution (e.g. Lesgourgues et al. 2007; Vikhlinin et al. 2009; Komatsu et al. 2011). The seven new runs use the following parameters: $\Omega_{\text{M},0} = 0.24$, $\Omega_{\Lambda,0} = 0.76$, $\Omega_{\text{B},0} = 0.04$, and $H_0 = 72 \text{ km s}^{-1} \text{ Mpc}^{-1}$. The two old runs (Barai et al. 2013) use $\Omega_{\text{M},0} = 0.2711$, $\Omega_{\Lambda,0} = 0.7289$, $\Omega_{\text{B},0} = 0.0463$, and $H_0 = 70.3 \text{ km s}^{-1} \text{ Mpc}^{-1}$. We assume that this slight change in cosmological parameters do not cause any difference in the results.

Two simulations, *E35nw* and *E35rvw*, are taken from Barai et al. (2013). The relevant numbers are $L_{\text{box}} = 25 h^{-1} = 35.56 \text{ Mpc}$ comoving, $N_{\text{part}} = 2 \times 320^3$, $m_{\text{gas}} = 8.72 \times 10^6 M_{\odot}$, $L_{\text{soft}} = 2.77 \text{ kpc}$. Here the minimum gas smoothing length is set to a fraction 0.001 of L_{soft} .

We perform six new runs: five varying the SN feedback parameters of MUPPI, and one with the effective model. These are with a box size of $L_{\text{box}} = 25 \text{ Mpc}$ comoving, using $N_{\text{part}} = 2 \times 256^3$ DM and gas particles in the initial condition, and gas particle mass $m_{\text{gas}} = 5.36 \times 10^6 M_{\odot}$. The Plummer equivalent softening length for gravitational forces is set to $L_{\text{soft}} = 2.08 \text{ kpc}$ comoving for the evolution up to $z = 2$. The softening is then held fixed at $L_{\text{soft}} = 0.69 \text{ kpc}$ in physical units from $z = 2$ to 0. We perform an additional MUPPI run with a larger box size of 50 Mpc comoving, with the same resolution, hence using $N_{\text{part}} = 2 \times 512^3$ DM and gas particles. The minimum gas smoothing length attainable is set to 0 in all our seven runs. In all cases, the minimum smoothing which is actually achieved in the simulations depends on the resolution, and in our runs the gas smoothing lengths went down to $\sim 0.2 L_{\text{soft}}$.

All the nine simulations incorporate the metal cooling and chemical enrichment subresolution physics described in Sections 2.1 and 2.2, and investigate different SF and SN feedback models, as summarized below.

(i) *E35nw* – effective model (Section 2.3), no wind, no kinetic SN feedback, run NW of Barai et al. (2013).

(ii) *E35rvw* – effective model, radially varying wind of velocity $v_w(r)$ (equation 4) with fixed parameter values described in Section 2.3, its speed going up to $v_{\text{max}} = 800 \text{ km s}^{-1}$, run RVW of Barai et al. (2013).

(iii) *E25cw* – effective model, energy-driven wind with constant velocity $v_w = 350 \text{ km s}^{-1}$.

(iv) *M25std* – MUPPI model (Section 2.4) of SF and SN feedback, ‘standard’ parameter values: $f_{\text{fb,out}} = 0.2$, $f_{\text{fb,kin}} = 0.6$, $P_{\text{kin}} = 0.03$.

(v) *M25a* – MUPPI model, higher thermal and lower kinetic feedback energy fraction: $f_{\text{fb,out}} = 0.4$, $f_{\text{fb,kin}} = 0.4$, $P_{\text{kin}} = 0.03$.

(vi) *M25b* – MUPPI model, higher kinetic feedback energy fraction: $f_{\text{fb,out}} = 0.2$, $f_{\text{fb,kin}} = 0.8$, $P_{\text{kin}} = 0.03$.

(vii) *M25c* – MUPPI model, less efficient kinetic feedback, lower probability of kicking gas particles into wind: $f_{\text{fb,out}} = 0.2$, $f_{\text{fb,kin}} = 0.6$, $P_{\text{kin}} = 0.01$.

(viii) *M25d* – MUPPI model, more efficient kinetic feedback, higher probability of kicking gas particles into wind: $f_{\text{fb,out}} = 0.2$, $f_{\text{fb,kin}} = 0.6$, $P_{\text{kin}} = 0.06$.

(ix) *M50std* – MUPPI model, larger box, standard parameter values: $f_{\text{fb,out}} = 0.2$, $f_{\text{fb,kin}} = 0.5$, $P_{\text{kin}} = 0.03$.

We compute the total gas metallicity, Z_{gas} , as the ratio of all metal mass to the total gas mass for each gas particle. Abundance ratios are expressed in terms of the solar metallicity, which is $Z_{\odot} = 0.0122$ (mass fraction of all metals in the Sun) derived from the compilation by Asplund, Grevesse & Sauval (2005).

3.1 Outflow measurement technique

We measure outflow of a galaxy by tracking the high-speed gas particles belonging to it. We identify haloes in the simulations using the friends-of-friends (FOF) group finder algorithm, which gives the virial radius R_{vir} . Subsequently we track galaxies using the subhalo finder `SUBFIND`, which identifies associated substructures to FOF haloes. The centre of each galaxy is considered as the location of the gravitational potential minimum of its subhalo. A minimum stellar mass of $10^9 M_{\odot}$ is used to select the galaxy population, corresponding to 750 star particles in the MUPPI model. Only the central galaxies are considered (not the satellites) for the outflow analysis. We define the *galaxy radius* of the centrals to be $R_{\text{gal}} = R_{\text{vir}}/10$. Each central galaxy having $M_* > 10^9 M_{\odot}$ is post-processed as described below. First the coordinates are transformed such that the cold gas disc of the galaxy is rotating in the $[X-Y]$ plane, and Z -axis is the perpendicular direction.

We aim to quantify the motion of gas particles caused by SN feedback, which are expected to move at speeds in excess of $\sim 300 \text{ km s}^{-1}$ in all models with kinetic feedback. Gas particles, in the form of hot gas or cold streams, will move within a DM halo with speeds of the order of the halo circular velocity, and typically below its escape velocity $v_{\text{esc}} = \sqrt{2GM_{\text{halo}}/R_{\text{vir}}}$ (for a galaxy halo mass M_{halo}); we will call these ‘virial’ motions. In order to quantify outflows one could estimate the mass outflow and inflow rate of all gas particles, and take their difference; this would single out SN-driven outflows as long as virial motions do not produce net changes in mass. This assumption may be correct in the inner parts of relatively small and slowly evolving DM haloes, but is surely incorrect when applied at the virial radius; in this case we would measure the net effect of outflows and cosmological infall.

Another option is to select only gas particles whose radial velocity is positive and exceeds v_{esc} . This option would have the merit of selecting outflowing gas particles that can make their way out of the halo, if hydrodynamical interactions with the halo gas do not slow them significantly. In less massive haloes, where v_{esc} is much smaller than the typical velocity of gas particles subject to kinetic feedback, such particles will clearly separate out in a radial

³ <http://camb.info/>

distance–radial velocity plot (e.g. fig. 2 of Barai et al. 2013). In more massive haloes, however, outflowing particles will have similar speeds as those subject to virial motion, and the distinction will be more difficult. In this case, a selection based on the escape velocity will have the merit to measure not the whole outflow, but the fraction that can truly escape the halo.

Any measure of average speed of outflowing particles, $\langle v_{\text{out}} \rangle$, will be affected by the assumed lower velocity threshold. As a consequence, we expect $\langle v_{\text{out}} \rangle$ to scale with halo mass when v_{esc} is used as a velocity threshold, even if kinetic feedback produced exactly the same velocities in all galaxies. Therefore, to study the relation of the average outflow velocity with respect to galaxy properties, we will use a fixed velocity threshold, and exclude all the haloes with escape velocity higher than that threshold since the measure there would be significantly affected by virial motions. A value of 300 km s^{-1} is a good compromise that allows us to measure outflows for many galaxies excluding only a few, most massive haloes. However, the quantification of the mass loading will be preferentially done using the escape velocity threshold.

We also need to define a volume around a galaxy where to measure the outflow, a region most expected to contain the gas ejected by SN feedback. The MUPPI subresolution model deposits thermal and kinetic energy from SN to neighbouring gas inside a cone with semi-aperture angle $\theta = 60^\circ$, therefore, to detect outflows we use two cylindrical volumes located above and below the galaxy and aligned with the galaxy disc. We use such cylindrical volumes to detect outflows in order to intercept the largest number of gas particles which have received SN feedback energy, and hence obtain a robust measurement. In addition, to better assess and quantify the geometry of the outflow, we also measure outgoing gas around a galaxy using a spherical shell around it. Most of our results in Section 4.3 utilize the bicylinder approach, except Section 4.3.3 where we apply the spherical shell technique.

Two cylindrical volumes are constructed, at a distance of R_{gal} above and below the galaxy disc plane, along the Z -direction. Each cylinder has a height of $h_{\text{cyl}} = R_{\text{gal}}$. The cylinder radius extends beyond R_{gal} , and the excess length subtends an angle of 60° with a plane perpendicular to the disc at R_{gal} . Mathematically, the cylinder radius is thus $(R_{\text{gal}} + R_{\text{gal}} \tan 60)$. The 60° angle is chosen to coincide with the opening angle within which gas particles are kicked during SN kinetic feedback of MUPPI subresolution model.

Lets denote that the i th gas particle has a mass m_i , z -velocity $v_{z,i}$, and lies at a z -coordinate of z_i . All the gas particles are selected, whose positions lie inside either cylinder, and moving at a high speed such that $|v_{z,i}| > v_{\text{lim, out}}$, or the z -magnitude of velocity is higher than a limiting speed. Here $v_{\text{lim, out}}$ can be a fixed value, or the escape velocity. The results in Section 4.3 are illustrated using both the limits for a few runs, and the final physical choices are described next. If the z -velocity is directed outward ($z_i v_{z,i} > 0$), then the gas particle is counted as outflow.

The outflow velocity, v_{out} , is estimated from $|v_z|$. One of our goals is to infer a physical galaxy property (e.g. mass, SFR) with which v_{out} correlates better. Selecting gas particles above v_{esc} brings in some inherent correlations between the resulting computed v_{out} and galaxy mass, because of the dependence of v_{esc} on M_{halo} by definition. Such built-in relations are unwanted and must be eliminated. Therefore, while calculating v_{out} , we choose a constant value as the limiting speed for selecting gas particles: $v_{\text{lim, out}} = 300 \text{ km s}^{-1}$. The mass-weighted average outflow velocity is determined as

$$\langle v_{\text{out}} \rangle = \frac{\sum_{i=1}^{n_{\text{out}}(|v_{z,i}| > 300)} |v_{z,i}| m_i}{\sum_{i=1}^{n_{\text{out}}(|v_{z,i}| > 300)} m_i}. \quad (10)$$

The limiting halo mass for which $v_{\text{esc}} = 300 \text{ km s}^{-1}$ is $M_{\text{halo, lim}} = 1.3 \times 10^{12} M_{\odot}$. Measuring v_{out} by selecting gas above 300 km s^{-1} ensures that outflows in galaxies less massive than $M_{\text{halo, lim}}$ can escape the halo potential, and might not escape away in galaxies more massive than $M_{\text{halo, lim}}$. This is accordingly noted in our analysis presented in Section 4.3.1.

On the other hand, the mass outflow rate, \dot{M}_{out} , should be evaluated over all the gas which can escape the galaxy total gravitational potential. Therefore, $v_{\text{lim, out}} = v_{\text{esc}}$ is used here. We calculate \dot{M}_{out} by summing over all the n_{out} gas particles having $|v_{z,i}| > v_{\text{esc}}$:

$$\dot{M}_{\text{out}} = \sum_{i=1}^{n_{\text{out}}(|v_{z,i}| > v_{\text{esc}})} \frac{m_i |v_{z,i}|}{h_{\text{cyl}}}. \quad (11)$$

We use a sphere technique for measuring outflows in Section 4.3.3. A spherical shell volume of thickness h_{sph} is constructed around each galaxy centre. The gas particles lying inside the spherical shell, and moving radially faster than the escape velocity at that radius, $|v_r| > v_{\text{esc}}(r)$, are selected. If the radial velocity is directed outward ($v_r > 0$) then the gas particle is counted as outflow. We calculate the mass outflow rate as

$$\dot{M}_{\text{out}} = \sum_{i=1}^{n_{\text{out}}} \frac{m_i |v_{r,i}|}{h_{\text{sph}}}. \quad (12)$$

For $r = R_{\text{gal}}$, the inner radius of the shell is located at a distance of R_{gal} from galaxy centre, $h_{\text{sph}} = R_{\text{gal}}$, and $|v_r| > v_{\text{esc}}(R_{\text{gal}})$ is used. For $r = R_{\text{vir}}$, the shell inner radius is at a distance $0.9R_{\text{vir}}$, $h_{\text{sph}} = 0.1R_{\text{vir}}$, and $|v_r| > v_{\text{esc}}(R_{\text{vir}})$ is used.

4 RESULTS AND DISCUSSION

4.1 Star formation rate density

The global star formation rate density (SFRD) as a function of redshift is plotted in Fig. 1, with the nine runs labelled by the different colours and plotting symbols. The SFRD (in $M_{\odot} \text{ yr}^{-1} \text{ Mpc}^{-3}$) is computed by summing over all the SF occurring in each simulation box at a time, and dividing it by the time-step interval and the box volume. Observational data ranges are shown as the grey shaded region, taken mainly from Cucciati et al. (2012), and the compilations therein originally from Perez-Gonzalez et al. (2005), Schiminovich et al. (2005), Bouwens et al. (2009, 2012), Reddy & Steidel (2009), Rodighiero et al. (2010), and van der Burg et al. (2010).

SN feedback clearly has a significant impact on the SFRD; compared to *E35nw*, SF is reduced by a factor of several in the other runs at $z < 8$. The stronger kinetic feedback runs (*M25b* and *M25d*) quench SFR more than the others. In fact, case *M25d* produces the lowest SFRD from high- z up to $z = 2$, but at $z < 2$ run *E25cw* has the lowest SFRD. Among the feedback runs, *M25c* produces the highest SFRD; implying that a 1 per cent probability of kicking gas particles into wind yields the least efficient kinetic feedback.

The scatter in the SFRD values within the MUPPI runs is larger at $z > 1$, and reduces at $z < 1$ due to overall gas depletion. The SFRD is higher in *M50std* than in *M25std* from high- z up to $z \sim 3$, and becomes comparable later. This is because, despite having the same parameter values and resolution, runs *M50std* and *M25std* use different cooling functions (Section 2.1).

At earlier cosmic epochs $z > 5$, the SFRD in the simulations is systematically higher, reaching 2–5 times the observed values. Later at $z < 5$, most of the models overall lie within the ranges of SFRD produced by the different observations. However at $z < 0.7$, the MUPPI models produce a higher and the effective model a lower

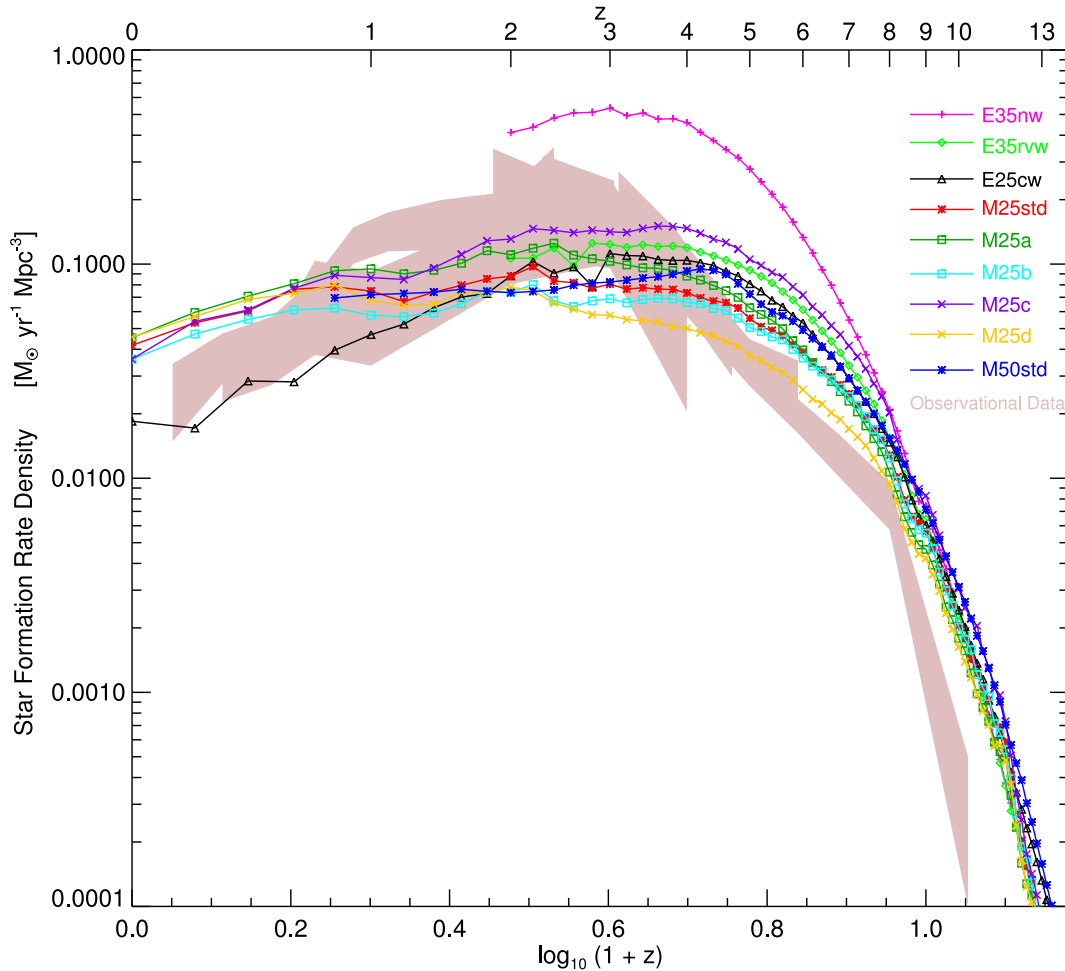


Figure 1. Total SFRD in simulation volume as a function of redshift, with the different models labelled by the colour and plotting symbol. The grey shaded region denotes a combination of observational data range from Cucciati et al. (2012), and the compilations therein originally from Perez-Gonzalez et al. (2005), Schiminovich et al. (2005), Bouwens et al. (2009, 2012), Reddy & Steidel (2009), Rodighiero et al. (2010), and van der Burg, Hildebrandt & Erben (2010). The comparison is described in Section 4.1.

SFRD than the observations. The low- z discrepancy is because we do not have AGN feedback, which when present is expected to quench additional SF, bringing the MUPPI models closer to observations. Studying the shape evolution, most of the simulations reach a maximum SFRD in the form of a plateau between $z = 2$ and 4 , and the SFRD decreases steeply at $z > 4$ and gradually at $z < 2$. This is contrary to the peak of observed SFRD at $z \sim 2$.

We compare our results with two contemporary cosmological hydrodynamical simulations. At $z \geq 3$ the SFRD in our simulations is higher than that obtained in Illustris (Vogelsberger et al. 2014), our SFRD exhibits a plateau maximum and not a well-defined peak at $z \sim 2$ like them, and at $z = 0$ also our SFRD is higher. Our results are more akin to that of some runs in OWLS (Schaye et al. 2010) which show a SFRD plateau between $z = 2$ and 4 .

4.2 Single galaxy

The gas distribution of a massive galaxy of total mass $M_{\text{halo}} = 3.4 \times 10^{12} M_{\odot}$ (left-hand two columns) and $1.8 \times 10^{12} M_{\odot}$ (remaining columns) at $z = 2$ is plotted in Fig. 2 for three runs. Each of the five rows shows a gas/star property, projected in the face-on (left) and edge-on (right) planes of a $(100 \text{ kpc})^3$ volume. First row depicts the velocity vectors of 7 per cent gas particles, with the outgoing

($v_r > 0$) particles denoted as red, and incoming ($v_r < 0$) gas as black. Here the blue circle in the face-on panels and the double blue rectangles in the edge-on panels illustrate the projected bicylinder volume used to measure the outflow (Section 3.1) of each galaxy. Gas density is in the second row, temperature in the third, and total metallicity is plotted in the fourth row.

E35nw and *M25std* present the formation of a gas disc with extended spiral arms and tidal features. In the no-wind case *E35nw*, the gas disc is bigger in size, more massive, more metal enriched; and there is no prominent outflow. While in run *E25cw* the central gas distribution is spheroidal, and most of the outflowing gas lies inside $r < 20 \text{ kpc}$, because here the wind kick velocity $v_w = 350 \text{ km s}^{-1}$ is too small to drive large-scale outflows. The MUPPI run *M25std* produces a well-developed gas outflow propagating perpendicular to the galaxy disc, escaping to $r > 30 \text{ kpc}$ from the galaxy centre. Metals are more distributed in runs *E25cw* and *M25std*, since SN winds carry the metals out from the SF regions and enrich the CGM. The fourth row also shows that the *M25std* outflow (right-hand two panels) is more metal enriched at 30 kpc from the galaxy than the *E25cw* case (middle two panels). Stellar mass in the bottom row reveals a central disc-like structure, surrounded by a larger stellar halo. The stellar disc is thinner in the no-wind case *E35nw* than in the MUPPI run *M25std*.

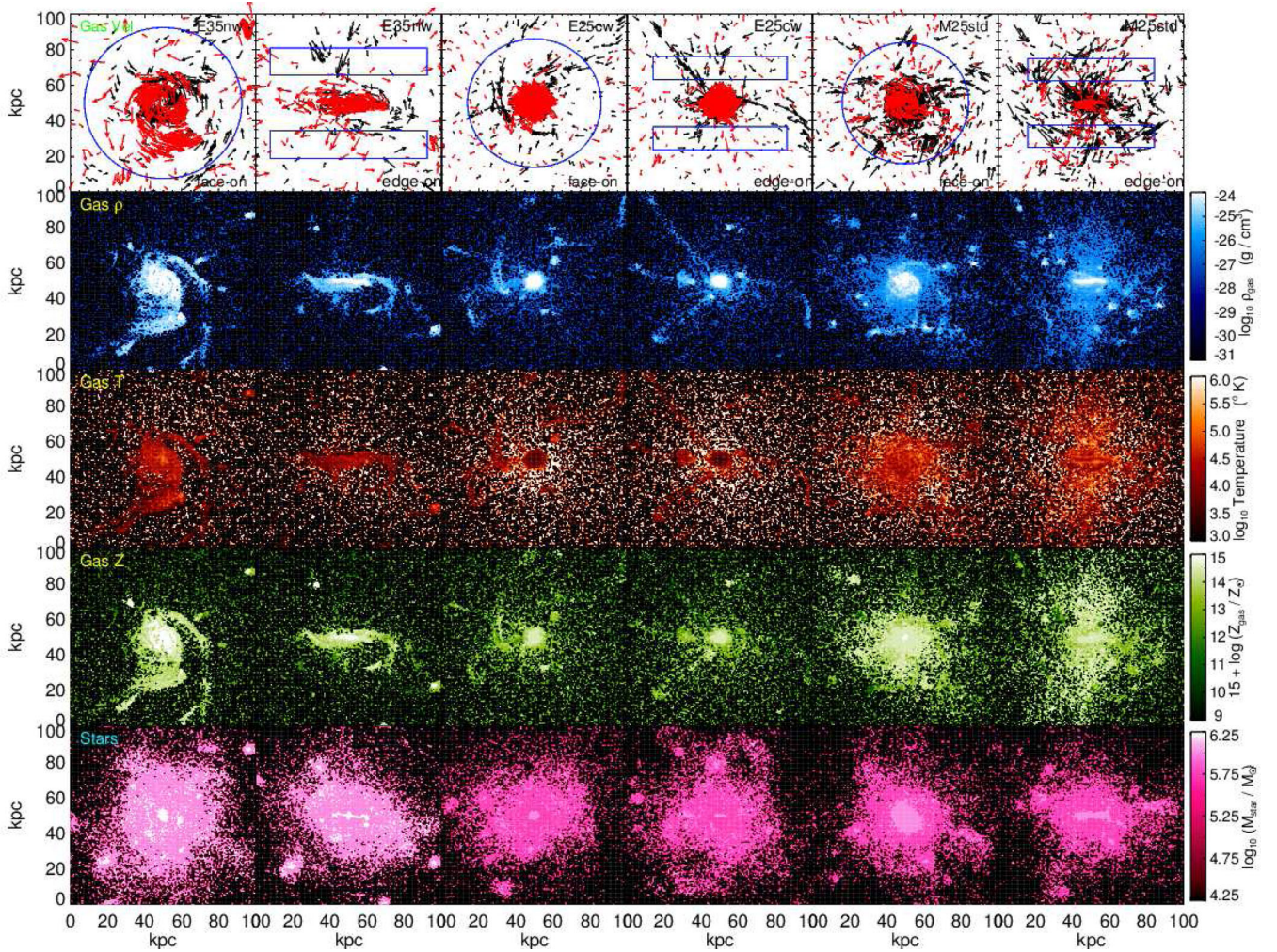


Figure 2. Projection of gas kinematics (top four rows) and stars (bottom row) in the face-on (left) and edge-on (right) planes of a $(100 \text{ kpc})^3$ volume centred around a massive galaxy at $z = 2$, in runs: *E35nw* (left-hand two columns), *E25cw* (middle two columns), and *M25std* (right-hand two columns). First row depicts the velocity vectors of 7 per cent of all the gas particles inside the plotted volume, with the outflowing ($v_r > 0$) particles denoted as red, and the inflowing ($v_r < 0$) as black. Second row shows gas density, third row is gas temperature, and fourth row is gas total metallicity. Bottom row presents the projected stellar mass. In the top row, the blue circle in the face-on panels and the double blue rectangles in the edge-on panels illustrate the projected bicylinder volume used to measure outflows.

4.3 Outflow properties of galaxies at $z = 2$

We measure the gas outflow properties of galaxies using the bicylinder technique described in Section 3.1, with a limiting velocity both fixed and scaled with v_{esc} , by analysing central galaxies having $M_* > 10^9 M_\odot$. The results of all the nine simulations at $z = 2$ are presented in this section.

We study the trends of outflow v_{out} and \dot{M}_{out} with basic galaxy properties: (i) halo mass, (ii) gas mass, (iii) stellar mass, (iv) SFR (sum of all the instantaneous SF occurring in the gas belonging to a galaxy), (v) gas consumption time-scale = gas mass/SFR, (vi) SF time-scale = stellar mass/SFR; attempting to find possible correlations. We find positive correlations of the outflow quantities with galaxy mass and SFR. However the correlation with galaxy SFR is the tightest, hence we present only these here.

4.3.1 Outflow velocity

The velocity of outflow, $\langle v_{\text{out}} \rangle$, as a function of halo mass of galaxies in run *M50std* is plotted in Fig. 3, illustrating the two different

methods of computing v_{out} . Outflowing gas particles are selected when their z -velocity component is above (i) a constant limiting speed or $|v_{z,i}| > 300 \text{ km s}^{-1}$ (equation 10) in the left-hand panel, and (ii) the escape velocity or $|v_{z,i}| > v_{\text{esc}}$ at the right, as described in Section 3.1. As a test we present the inflows: gas particles having velocities over the threshold and $z_i v_{z,i} < 0$, as well in this figure. The flow direction is indicated by the plotting symbols: outflows as diamonds, and inflows as plus symbols. The plotting colour depicts the number fraction of galaxies where outflow or inflow is detected in bins of halo mass. The grey points in the left-hand panel (includes both outflow and inflow) mark galaxies more massive than $M_{\text{halo,lim}} = 1.3 \times 10^{12} M_\odot$ (vertical black dashed line). In the right-hand panel the inflow velocities are spread very close to the v_{esc} curve, because inflows consist of thermal velocity and random motion of the gas, and by imposing a lower cut-off of v_{esc} we measure the motion occurring close to v_{esc} . Whereas most the outflow velocities are larger (by a few times) than v_{esc} at all halo masses; which demonstrates that we are measuring non-thermal gas outflow driven by stellar and SN feedback processes. The left-hand panel, by selecting gas above a fixed cut-off of 300 km s^{-1} , shows

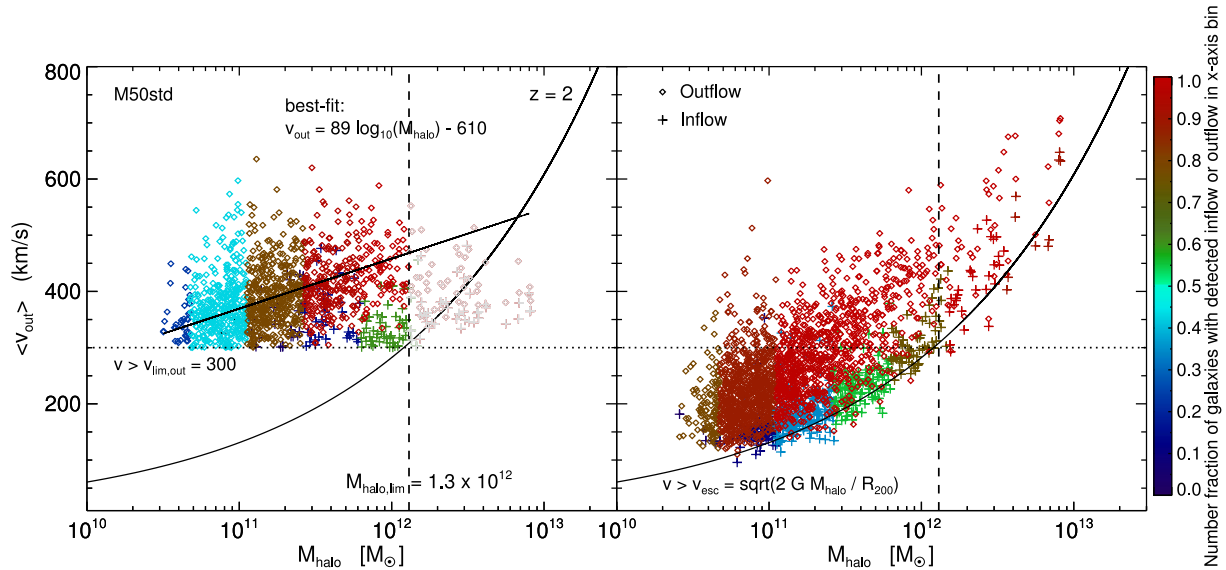


Figure 3. Outflow velocity mass-weighted average, $\langle v_{\text{out}} \rangle$, as a function of halo mass of galaxies in run *M50std*. The two panels show different methods of computing v_{out} , by selecting gas particles above: a constant limiting speed $|v_{z,i}| > 300 \text{ km s}^{-1}$ (horizontal black dotted line) in the left (equation 10 in Section 3.1), and the escape velocity $|v_{z,i}| > v_{\text{esc}}$ (black solid curve) at the right. Each point is one galaxy, and the plotting symbol indicates the flow direction of the measurements: outflows are denoted by diamonds, inflows by plus symbols. The plotting colour depicts the number fraction of galaxies where outflow or inflow is detected in bins of halo mass. The grey points in the left-hand panel (includes both outflow and inflow) mark galaxies more massive than $M_{\text{halo,lim}} = 1.3 \times 10^{12} M_{\odot}$ (vertical black dashed line), where the outflows might not escape the halo potential. Details in Section 4.3.1.

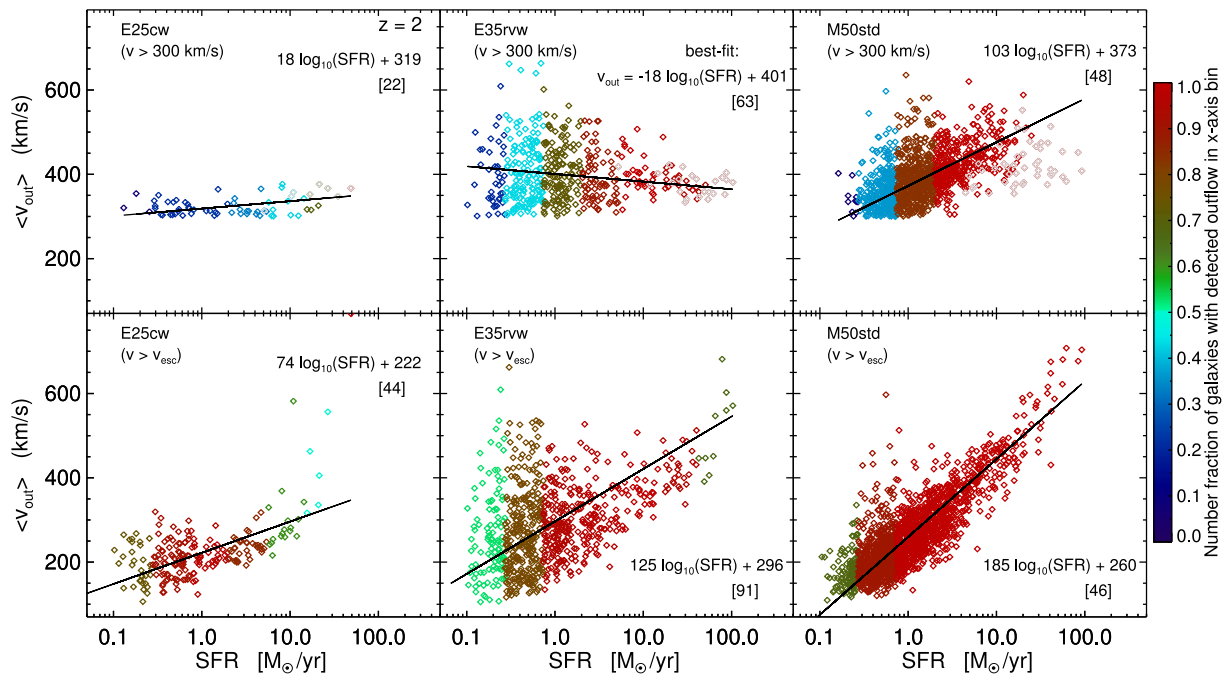


Figure 4. Outflow velocity as a function of SFR of galaxies in three runs: *E25cw* in the left-hand column, *E35rvw* at the middle, and *M50std* in the right. The two rows show different methods of computing outflow, by selecting gas particles above: a constant limiting speed $|v_{z,i}| > 300 \text{ km s}^{-1}$ at the top, and the escape velocity $|v_{z,i}| > v_{\text{esc}}$ in the bottom. The plotting colour depicts the number fraction of galaxies where outflow is detected in bins of galaxy SFR. The grey points in the top row mark galaxies more massive than $M_{\text{halo,lim}} = 1.3 \times 10^{12} M_{\odot}$, where the outflows might not escape the halo potential. The black line is the best-fitting relation between v_{out} and $\log_{10}(\text{SFR})$ obtained by an outlier-resistant two-variable linear regression. The fit coefficients and the ‘standard deviation’ of the fit’s residuals (within square brackets) are written inside the panels, using units same as the plotted axes.

a positive correlation of the measured outflow velocity with halo mass.

The outflow velocity as a function of SFR of galaxies is plotted in Fig. 4 for three runs, illustrating the two different methods of com-

puting outflow in the two rows. The plotting colour depicts the number fraction of galaxies where outflow is detected in bins of SFR, as indicated by the colour bar on the right. The differences between the two rows are the largest for the effective models *E25cw* and

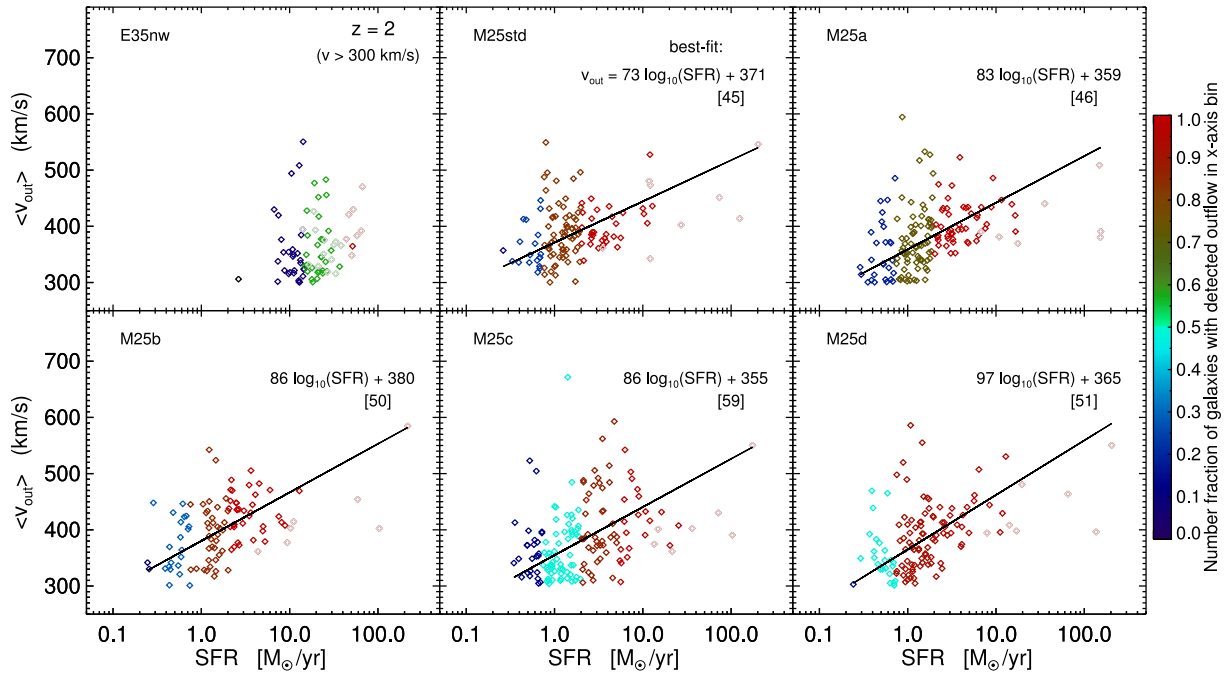


Figure 5. Outflow velocity as a function of SFR of galaxies for six simulations, one in each panel. The format is the same as the top row of Fig. 4. The plotting colour depicts the number fraction of galaxies where outflow is detected in bins of SFR. The grey points mark galaxies more massive than $M_{\text{halo, lim}} = 1.3 \times 10^{12} M_{\odot}$, where the outflows might not escape the halo potential. The black line in the latter five panels is the best-fitting relation between v_{out} and $\log_{10}(\text{SFR})$.

E35rvw (left-hand two columns), because these runs have energy-driven wind where v_w is not dependent on galaxy mass. *E25cw* has $v_w = 350 \text{ km s}^{-1}$, and using a fixed lower cut-off of 300 km s^{-1} selects only a few gas particles in the lower mass galaxies. For the MUPPI run *M50std*, the two distinct lower cut-offs make a small difference.

Fig. 5 presents the outflow velocity as a function of SFR of galaxies for the six remaining simulations, where outflow is measured by selecting gas above a fixed $|v_{z,i}| > 300 \text{ km s}^{-1}$. The grey points mark galaxies more massive than $M_{\text{halo, lim}} = 1.3 \times 10^{12} M_{\odot}$, where the outflows might not escape the halo potential.

We see that kinetic SN feedback is needed to generate an outflow in the lower SFR (consequently less massive) galaxies. Therefore the no-wind run *E35nw* shows outflowing gas only in some galaxies with $\text{SFR} > 8 M_{\odot} \text{ yr}^{-1}$; this can be interpreted as the expected contamination from gravity-driven gas flows, and is roughly consistent with the statistics of inflows in the left-hand panel of Fig. 3. In the other runs more than 50 per cent galaxies with $\text{SFR} \geq 1 M_{\odot} \text{ yr}^{-1}$ have outflows. The number fraction of galaxies where outflow is detected (indicated by the plotting colour) increases with galaxy SFR.

All the runs, except *E25cw*, present a large scatter. The effective models produce, with low probability, an outflow velocity which shows no relation with SFR. Run *E25cw* has a constant $v_{\text{out}} \sim 300 \text{ km s}^{-1}$, since the input model is energy-driven wind with a fixed $v_w = 350 \text{ km s}^{-1}$. Run *E35rvw* has a large scatter with $v_{\text{out}} \sim 300\text{--}500 \text{ km s}^{-1}$. It uses a radially varying wind of velocity $v_w(r)$ (equation 4) with the speed going up to $v_{\text{max}} = 800 \text{ km s}^{-1}$ at $R_{\text{eff}} = 100 h^{-1} \text{ kpc}$. This turns out to be a strong wind for the low-SFR galaxies, where $v_{\text{out}} \sim 650 \text{ km s}^{-1}$ is reached.

The six MUPPI runs (five in Fig. 5 and one in Fig. 4) display a positive correlation of v_{out} with galaxy SFR: v_{out} rising from 300 km s^{-1} at low SFR to $\sim 600 \text{ km s}^{-1}$ at high SFR. It is the most steep in the larger box run *M50std*, which has the highest number

of galaxies. The positive correlation has the largest scatter in *M25c*, the least efficient kinetic feedback case with a 1 per cent probability of kicking gas particles into wind.

4.3.2 Mass outflow rate

The mass outflow rate, \dot{M}_{out} from equation (11) in Section 3.1, as a function of SFR of galaxies, is plotted in Fig. 6 for three runs, illustrating the two different methods of computing outflow in the two rows. Gas particles are selected above: (i) a constant limiting speed $|v_{z,i}| > 300 \text{ km s}^{-1}$ in the top row, and (ii) the escape velocity $|v_{z,i}| > v_{\text{esc}}$ at the bottom. It is physically expected that gas moving faster than v_{esc} is able to escape the galaxy halo; therefore, the bottom row gives a physically motivated estimate of the outflowing mass that can make its way out of the halo. The difference between the two rows is the largest for run *E25cw* in the left-hand column; because it has energy-driven wind with $v_w = 350 \text{ km s}^{-1}$, and using a fixed lower cut-off of 300 km s^{-1} selects only a few gas particles in the lower mass galaxies. For the other two runs with strong kinetic feedback, *E35rvw* and *M50std*, the two distinct lower cut-offs make very small difference.

The mass outflow rate as a function of SFR of galaxies for the six remaining simulations is plotted in Fig. 7. The format is same as the bottom row of Fig. 6, where gas is selected above the escape velocity $|v_{z,i}| > v_{\text{esc}}$. The plotting colour depicts the number fraction of galaxies where outflow is detected in bins of galaxy SFR.

The no-wind run *E35nw* presents outflow in a few high-SFR galaxies only, and \dot{M}_{out} shows a scatter having no relation with the SFR. The two effective models with kinetic SN feedback (Fig. 6) display a weak positive correlation of \dot{M}_{out} and galaxy SFR, having a value of slope 0.86, which is flatter than the MUPPI models. *E25cw* has a larger scatter than *E35rvw*.

The six MUPPI runs (five in Fig. 7 and one in Fig. 6) exhibit a prominent positive correlation of \dot{M}_{out} with galaxy SFR, having

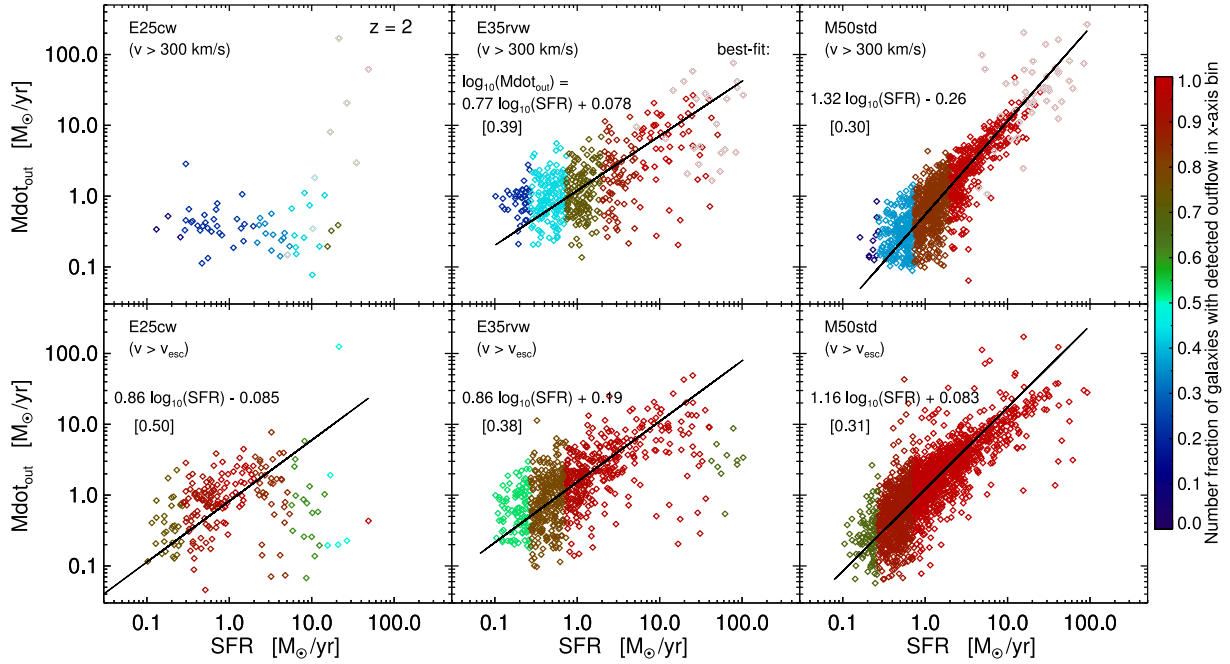


Figure 6. Mass outflow rate, \dot{M}_{out} from equation (11), as a function of SFR of galaxies in three runs: *E25cw* in the left-hand column, *E35rvw* at the middle, and *M50std* in the right. The two rows show different methods of computing outflow, by selecting gas particles above: a constant limiting speed $|v_{z,i}| > 300 \text{ km s}^{-1}$ at the top, and the escape velocity $|v_{z,i}| > v_{\text{esc}}$ in the bottom. The plotting colour depicts the number fraction of galaxies where outflow is detected in bins of galaxy SFR. The grey points in the top row mark galaxies more massive than $M_{\text{halo, lim}} = 1.3 \times 10^{12} \text{ M}_{\odot}$, where the outflows might not escape the halo potential. The black line in the latter five panels is the best-fitting relation between \dot{M}_{out} and SFR, with the coefficients of an outlier-resistant two-variable linear regression written inside the panels. Details in Section 4.3.2.

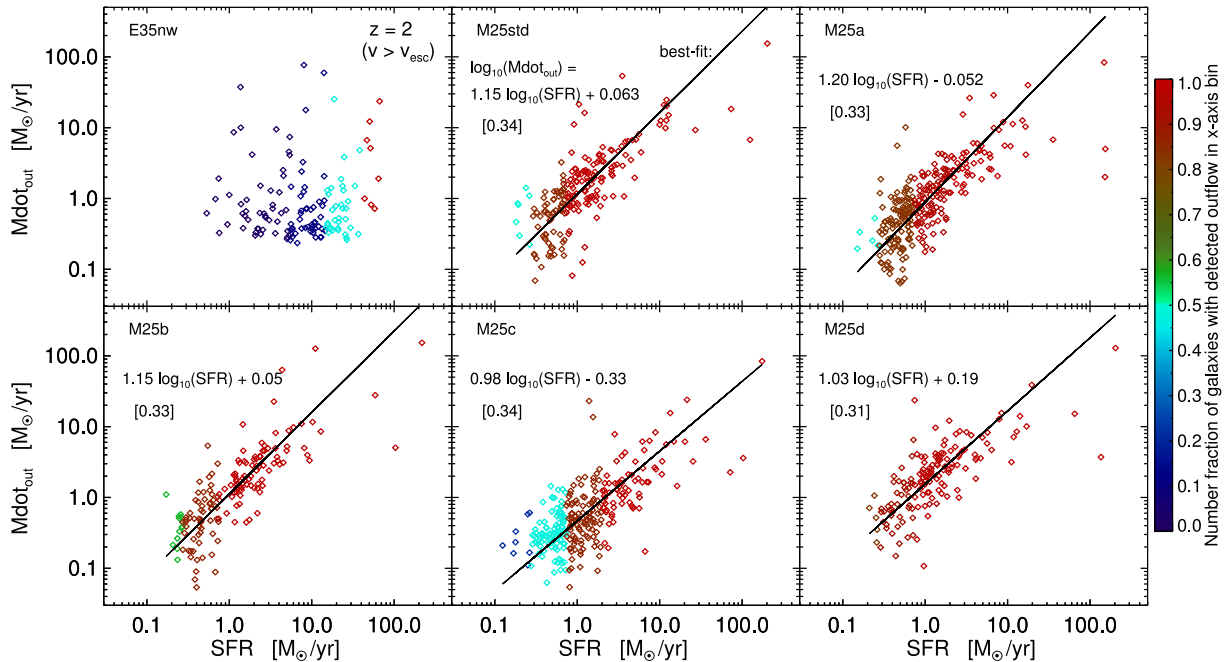


Figure 7. Mass outflow rate as a function of SFR of galaxies, for six simulations one in each panel. The format is the same as the bottom row of Fig. 6. The plotting colour depicts the number fraction of galaxies where outflow is detected in bins of galaxy SFR. The black line in the latter five panels is the best-fitting relation between \dot{M}_{out} and SFR. Details in Section 4.3.2.

slope values between 1 and 1.2. \dot{M}_{out} rises from $0.08 \text{ M}_{\odot} \text{ yr}^{-1}$ at low SFR to $50 \text{ M}_{\odot} \text{ yr}^{-1}$ at high SFR. All the runs present some scatter, with \dot{M}_{out} varying up to 10 times for the same SFR values.

4.3.3 Mass escape at virial versus galaxy radius

We compare outflow measurements at R_{gal} using the cylinder and the sphere techniques, which reveal us their shapes. During propagation an outflow could be slowed down by hydrodynamical interactions

Table 2. Number statistics of outflows in run *M50std* at $z = 2$ using different techniques, described in Section 4.3.3. Flows measured by tracking gas particles having a radial velocity higher than the escape: $|v_r| > v_{\text{esc}}(r)$. Column (1): method description. Column (2): N_{outflow} = number of galaxies where outflow is detected. Column (3): fraction $f_{\text{outflow}} = N_{\text{outflow}}/N_{\text{central}}$.

Method (1)	N_{outflow} (2)	f_{outflow} (3)
At R_{gal} using $ v_r > v_{\text{esc}}(R_{\text{gal}})$, in a cylinder	1842	0.93
At R_{gal} using $ v_r > v_{\text{esc}}(R_{\text{gal}})$, in a sphere	1936	0.97
At R_{vir} using $ v_r > v_{\text{esc}}(R_{\text{vir}})$, in a sphere	1734	0.87

with neighbouring gas. In order to estimate what mass fraction can escape the halo gravitational potential, we compare the rates by measuring outflow at the galaxy radius R_{gal} and that at the virial radius R_{vir} .

Here we present results of run *M50std* at $z = 2$ by analysing $N_{\text{central}} = 1986$ central galaxies, among a total of 2688 galaxies with $M_* > 10^9 M_{\odot}$. Table 2 lists the number of outflows detected using different methods at two radii: $r = R_{\text{gal}}$ in the first two rows, and $r = R_{\text{vir}}$ in the third row. We find that the fraction of galaxies where outflow is detected at R_{gal} is $f_{\text{outflow}} = 0.93$ using the cylinder method, and rises to 0.97 using the sphere technique. We furthermore find that the outflow detection fraction decreases from $f_{\text{outflow}} = 0.97$ at R_{gal} to 0.87 at R_{vir} . The reduction factor is small; among the outflows which escape the galaxy, ~ 90 per cent can escape the halo as well.

Fig. 8 presents the mass outflow rate in run *M50std* at $z = 2$ measured by different techniques; left-hand panel: at the galaxy radius R_{gal} in a sphere versus that at R_{gal} in a cylinder, and right-hand panel: at the virial radius R_{vir} in a sphere versus that at R_{gal} in a cylinder. Outflows are measured by selecting gas particles above the escape velocity $|v_{z,i}| > v_{\text{esc}}(r)$ at the given radius. There is a substantial scatter in the right-hand panel, with $\dot{M}_{\text{out}}(R_{\text{vir}})$ varying up to a few 10s at the same $\dot{M}_{\text{out}}(R_{\text{gal}})$; however, a clear positive correlation is visible. The black line shows the result of an outlier-resistant two-variable linear regression. In the right-hand panel, this gives the best-fitting relation of the mass escape at the two radii: $\dot{M}_{\text{out}}(R_{\text{vir}}) = 0.66\dot{M}_{\text{out}}(R_{\text{gal}})^{0.98}$. From the left-hand panel and the detection number ratio in the previous paragraph we conclude that the shape of the outflow is bi-polar in ~ 95 per cent galaxies.

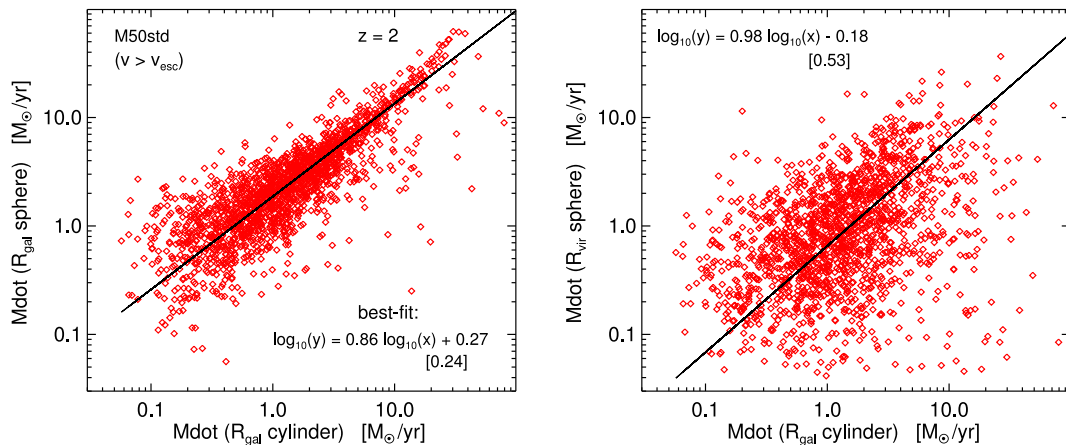


Figure 8. Mass outflow rate in run *M50std* at $z = 2$ measured by different techniques; left-hand panel: at the galaxy radius R_{gal} in a sphere (equation 12) versus that at R_{gal} in a cylinder, and right-hand panel: at the virial radius R_{vir} in a sphere versus that at R_{gal} in a cylinder. The black line shows the result of an outlier-resistant two-variable linear regression giving the best-fitting relation between the plotted quantities. The fit coefficients and the ‘standard deviation’ of the fit’s residuals (within square brackets) are written inside the panels, using units same as the plotted axes. Described in Section 4.3.3.

4.3.4 Mass loading factor

We compute the outflow mass loading factor η by taking the ratio of the mass outflow rate (measured at R_{gal} using the bicylinder method) with galaxy SFR:

$$\eta = \frac{\dot{M}_{\text{out}}}{\text{SFR}}. \quad (13)$$

Fig. 9 presents η as a function of halo mass of galaxies for all nine simulations, using a format same as Fig. 7. The outflowing gas is selected above the escape velocity $|v_{z,i}| > v_{\text{esc}}$. The plotting colour depicts the number fraction of galaxies where outflow is detected in bins of halo mass. All the runs exhibit a scatter, with η varying up to factors of some 10s at the same halo mass.

The effective model cases (*E35nw*, *E25cw*, and *E35rvw* at higher masses) generate a negative correlation of η with M_{halo} . This is because two runs have kinetic SN feedback in the energy-driven outflow formalism (Section 2.3), where the wind kick velocity v_w is fixed over all galaxy masses. The result turns out to be a strong wind for the low-mass galaxies, where a large amount of gas is expelled compared to SF, reaching $\eta \sim 10$. On the other hand, it is a weak wind for the high-mass galaxies, where little gas is expelled and $\eta \sim 0.01$. At lower masses ($M_{\text{halo}} < 4 \times 10^{11} M_{\odot}$), run *E35rvw* shows a constant η scattered between 0.4 and 10 versus M_{halo} .

All the six MUPPI runs display an almost constant value of η over the full range of M_{halo} . The mass loading factors in most of the MUPPI galaxies lie between $\eta = 0.2$ and 10, with an average value of $\eta \sim 1$.

4.3.5 Implications and comparison with theoretical estimates

We find that the MUPPI model is able to produce galactic outflows whose velocity and mass outflow rate correlates positively with global properties of the galaxy (halo mass, SFR). This is achieved with MUPPI using fully local properties of gas as input to the sub-resolution model. This trend, tracing some of the global properties of galaxy using local properties of gas, is found for the first time in cosmological simulations using subresolution models. We decipher that such trends arise from the details of the MUPPI subresolution model. Here SF depends on local pressure through the molecular fraction of gas (equation 5 in Murante et al. 2010), and the

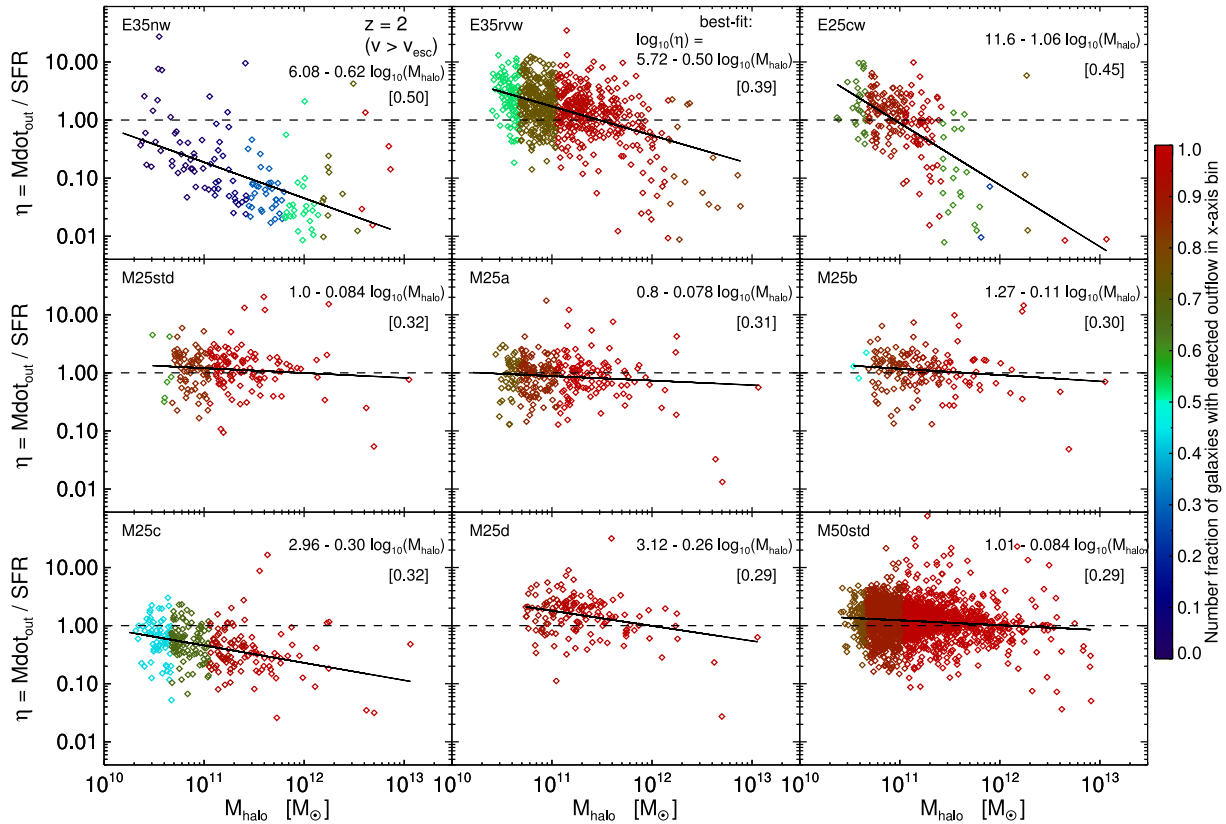


Figure 9. Mass loading factor, η from equation (13), as a function of halo mass of galaxies. Each of the nine panels shows one simulation. The format is the same as Fig. 7, where outflowing gas is selected above the escape velocity $|v_{z,i}| > v_{\text{esc}}$. The plotting colour depicts the number fraction of galaxies where outflow is detected in bins of halo mass. Details in Section 4.3.4.

gas pressure is expected to depend on halo mass. The star-forming gas undergoes kinetic feedback and produces galactic outflows. Therefore consequently the outflow properties become dependent on halo mass and other global properties, through the local gas pressure.

On the other hand, the effective model imparts a constant velocity v_w to the gas, and a constant mass loading $\eta = 2$, as input to the subresolution recipe. Consequently, the measured outflow speed is seen to be constant in the effective model. However, it produces a trend of η decreasing (from a value of 10 to 0.01) with halo mass, and $\eta = 2$ is only achieved for a narrow range of galaxy masses.

The results we obtain here by computing outflows in galaxies extracted from cosmological hydrodynamical simulations, can be compared to theoretical estimates of the MUPPI subresolution model. At variance with other kinetic wind recipes in the literature, in MUPPI neither the wind mass loading factor nor the wind velocity is given as input quantities. Nevertheless, typical values of these can be estimated using certain hypothesis about the average properties of the gas, as done by Murante et al. (2015) in their section 3.3. With the default parameter choices, the theoretical estimates are (equations 8 and 9 in Section 2.4) $\eta_{\text{th}} \simeq 1.5$, and the mass-weighted average wind velocity $v_{\text{wind,th}} \simeq 600 \text{ km s}^{-1}$. However, the exact values depend on the local dynamical time, hence in turn on the local gas properties.

The MUPPI runs *M25std* and *M50std* yield outflow mass loading factor between $\eta = 0.3$ and 8, with an average value of $\eta \simeq 1.2$, close to $\eta_{\text{th}} \simeq 1.5$. The outflow velocity shows a positive correlation with galaxy mass and SFR, v_{out} rising from 300 to 600 km s^{-1} . Hence the simulation v_{out} agrees with the theoretical estimate in higher

mass galaxies, but at lower masses the outflow speed is smaller than $v_{\text{wind,th}} \simeq 600 \text{ km s}^{-1}$.

The product of mass loading factor and outflow velocity squared is predicted to be a constant in the MUPPI model (Murante et al. 2015): $\eta_{\text{th}} v_{\text{wind,th}}^2 = f_{\text{fb,kin}} E_{\text{SN}} / M_{\text{*,SN}}$. This product for the simulated galaxies $\eta(v_{\text{out}})^2$ as a function of halo mass is plotted in Fig. 10 for run *M50std*. Here outflows are measured by selecting gas particles above the escape velocity $|v_{z,i}| > v_{\text{esc}}$. The horizontal black solid line marks the theoretical estimate $\eta_{\text{th}} v_{\text{wind,th}}^2 = 5.4 \times 10^5 \text{ km}^2 \text{ s}^{-2}$. The simulation results are lower than the theoretical prediction, especially in the less massive galaxies. This is because the prediction assumes certain average properties of the gas. We in turn conclude that only a fraction one-third of the deposited SN energy is used to drive an outflow; the rest being dispersed and radiated away through hydrodynamical interactions and by giving energy to slow particles.

4.4 Redshift evolution of outflows: from $z = 5$ to $z = 1$

The outflow detection fraction of run *M50std* as a function of redshift is plotted in Fig. 11. Left-hand panel shows the absolute number of central galaxies in simulation volume having a stellar mass $M_{\text{*}} > 10^9 M_{\odot}$. Right-hand panel illustrates the number fraction of these centrals where outflow is detected (defined in Table 2), using the cylindrical volume methodology of Section 3.1. When outflow is measured by selecting gas above the escape velocity ($|v_{z,i}| > v_{\text{esc}}$, asterisks, blue curve), the outflow detection fractions are high at all epochs, reducing gradually from $f_{\text{outflow}} = 0.99$ at $z = 5$, to 0.8 at $z \sim 1$. When measured above a constant limiting

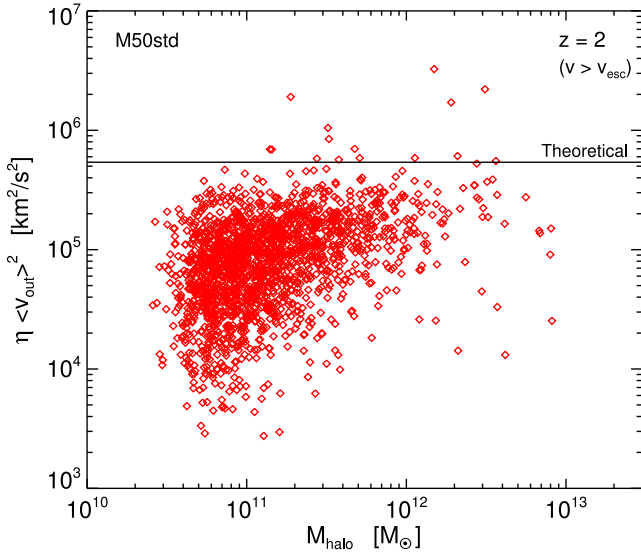


Figure 10. Product of mass loading factor and outflow velocity squared, $\eta\langle v_{\text{out}}\rangle^2$, as a function of halo mass of galaxies, in run *M50std*. Outflows measured by selecting gas particles above the escape velocity $|v_{z,i}| > v_{\text{esc}}$. The horizontal black solid line marks the theoretical estimate $\eta_{\text{th}}v_{\text{wind,th}}^2$ (Murante et al. 2015). Description in Section 4.3.5.

speed ($|v_{z,i}| > 300 \text{ km s}^{-1}$, diamonds, red curve), f_{outflow} decreases from 0.8 at $z = 4$, to 0.4 at $z \sim 1$.

The redshift evolution of outflow velocity in simulation run *M50std* as a function of SFR of galaxies is plotted in Fig. 12. It shows the mass-weighted average, $\langle v_{\text{out}}\rangle$ from equation (10) in Section 3.1. Each point is one galaxy, and the five panels show different redshifts. The remaining plotting format is the same as in Fig. 5. The correlation between v_{out} and SFR is positive at all the explored epochs: steeper at earlier times, and becomes flatter at later epochs. The best-fitting slope of v_{out} (km s^{-1}) versus $\log_{10}(\text{SFR}/M_{\odot} \text{ yr}^{-1})$ are 155, 163, 144, 103, 43 at $z \sim 5, 4, 3, 2, 0.8$.

The redshift evolution of mass loading factor of galaxies in run *M50std* as a function of halo mass is plotted in Fig. 13. It shows η from equation (13), as in Fig. 12, presenting the simulation at different epochs. In this figure the plotting colour depicts the number fraction of galaxies where outflow is detected in bins of halo mass. The value of η exhibits a scatter at all the epochs, varying up to

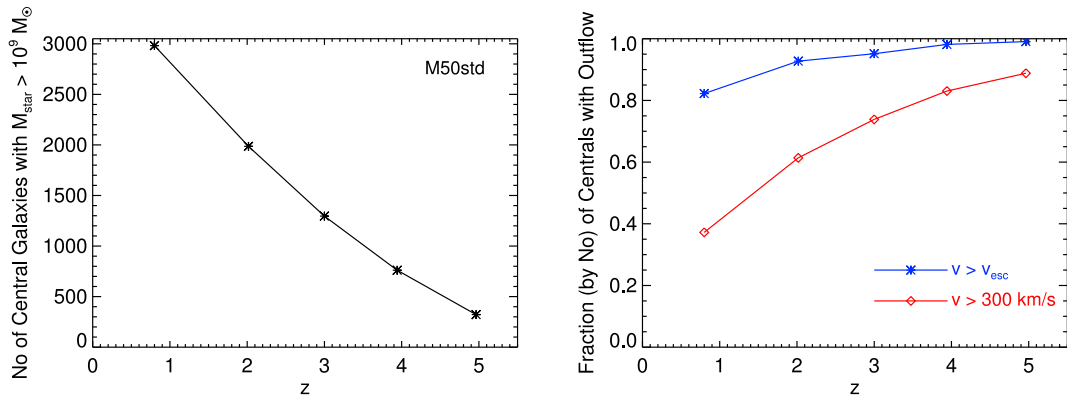


Figure 11. Number of central galaxies in run *M50std* having a stellar mass $M_{\star} > 10^9 M_{\odot}$ in the left-hand panel, and number fraction of these centrals where outflow is detected at the right, as a function of redshift. The two curves in the right-hand panel indicate different methods of measuring outflow (Section 3.1), by selecting gas above: a constant limiting speed $|v_{z,i}| > 300 \text{ km s}^{-1}$ (diamonds, red curve), and the escape velocity $|v_{z,i}| > v_{\text{esc}}$ (asterisks, blue curve). Description in Section 4.4.

factors of 10 at the same halo mass. Earlier on between $z = 2$ and 5, the galaxies have an almost constant value of η over the full range of M_{halo} . The mass loading factors lie within $\eta = 0.1\text{--}20$, with an average value decreasing with the passage of time. At later epochs $z = 0.8$, η displays a negative correlation with M_{halo} at the high-mass end.

The most important factor causing these redshift evolution of the outflow properties is the decrease of SFR at low- z (Section 4.1). As seen in Fig. 1, the global SFRD in run *M50std* reaches a maximum between $z = 2$ and 4 in the form of a plateau, with a steeper reduction of SFRD at earlier and later redshifts. This high SFR activity drives strong outflows in a greater fraction of galaxies, and causes the positive correlation of v_{out} with SFR, as well as the constant η trend. Later at $z \leq 1$, SFR in galaxies reduce due to overall gas depletion, hence the driven outflows become weaker and rarer, and the outflow correlations are lost.

4.5 Comparison of outflows with observations and other models

Observational signatures of galactic outflows mostly composed of single-galaxy detections. As a recent example at high redshift, Crighton et al. (2015) observed absorbing gas clumps in a $z = 2.5$ galaxy CGM, produced by a wind with a mass outflow rate of $\sim 5 M_{\odot} \text{ yr}^{-1}$. At low redshift, Cazzoli et al. (2014) detected kpc-scale neutral gas outflowing perpendicular to the disc of a $z = 0.01$ galaxy, at a rate $\sim 48 M_{\odot} \text{ yr}^{-1}$, with a global mass loading factor $\eta \approx 1.4$. Such values of mass outflow rate (a few to 10s $M_{\odot} \text{ yr}^{-1}$) and η lie within our simulation result range (Sections 4.3.2 and 4.3.4).

Only over the last few years, observations of outflows in galaxy populations have been possible, and subsequent derivation of systematic trends. Grimes et al. (2009) detected starburst-driven galactic winds of temperature $10^{5.5} \text{ K}$ in the absorption spectra of 16 local galaxies, and found that v_{out} increases with both the SFR and the SFR per unit stellar mass. In a spectroscopic catalogue of 40 luminous starburst galaxies at $0.7 \leq z \leq 1.7$, Banerji et al. (2011) inferred the presence of large-scale outflowing gas, with $v_{\text{out}} \propto \text{SFR}^{0.3}$. Analysing the cool outflow around galaxies at $1 \leq z \leq 1.5$, Bordoloi et al. (2013) found that v_{out} (ranging between 200 and 300 km s^{-1}) increases steadily with increasing SFR and stellar mass, and the wind is bipolar in geometry for disc galaxies. At low redshifts, Martin (2005) observed a positive correlation of outflow speed with

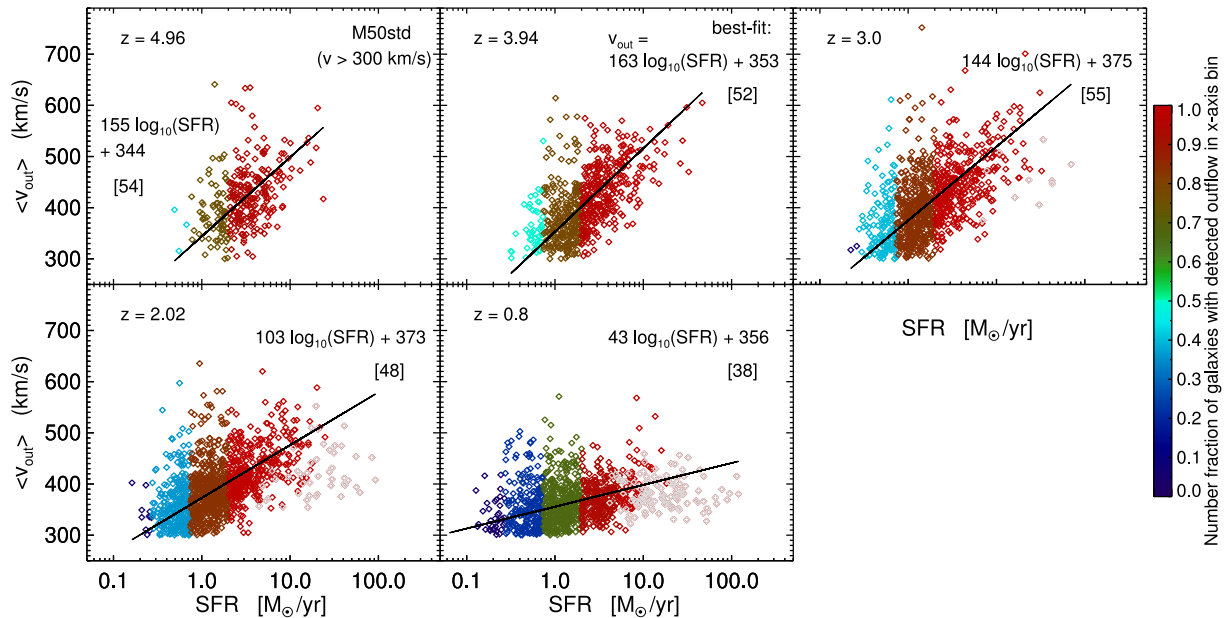


Figure 12. Redshift evolution of outflow velocity mass-weighted average, $\langle v_{\text{out}} \rangle$ from equation (10), as a function of SFR of galaxies. Here outflowing gas is selected above a constant limiting speed $|v_{z,i}| > 300 \text{ km s}^{-1}$. Each point is one galaxy of simulation run *M50std*, and the five panels show epochs of $z \sim 5, 4, 3, 2, 0.8$. The plotting colour depicts the number fraction of galaxies where outflow is detected in bins of galaxy SFR. The grey points mark galaxies more massive than $M_{\text{halo, lim}} = 1.3 \times 10^{12} M_{\odot}$, where the outflows might not escape the halo potential (Section 3.1). Discussed in Section 4.4.

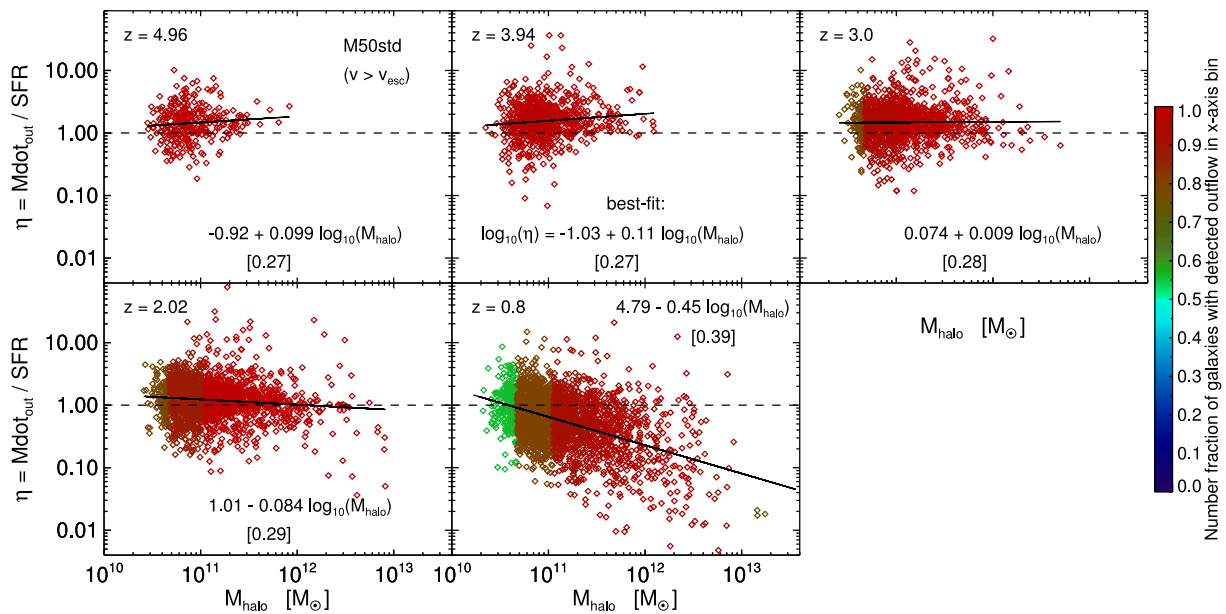


Figure 13. Redshift evolution of mass loading factor, η from equation (13), as a function of halo mass of galaxies. The format is the same as Fig. 12, showing simulation *M50std* at different epochs. Except here the outflowing gas is selected above the escape velocity $|v_{z,i}| > v_{\text{esc}}$. The plotting colour depicts the number fraction of galaxies where outflow is detected in bins of halo mass. Details in Section 4.4.

galaxy mass in ultraluminous infrared galaxies at $z = 0.042\text{--}0.16$. Our simulations predict a positive correlation of v_{out} with galaxy SFR and halo mass (Section 4.3.1), especially at $z \geq 2$ (Section 4.4); hence consistent with all these observations.

Some galaxies in our simulations have a large $v_{\text{out}} \sim 500\text{--}700 \text{ km s}^{-1}$. This is in agreement with the high-velocity (480–651 km s^{-1}) outflow observations by Karman et al. (2014) at $z \sim 3$ in the UV spectra of massive galaxies. Our simulated trend that the outflow detection fraction decreases from $z = 3$ to 0.8 (Sec-

tion 4.4) is consistent with that observed by Karman et al. (2014): the incidence of high- v_{out} outflows (40 per cent) is much higher at $z \sim 3$ massive galaxies than those at $z < 1$; which is justified by the powerful SF and nuclear activity that most massive galaxies display at $z > 2$.

An earlier simulation work by Oppenheimer & Davé (2008) yielded galactic outflows with faster wind speeds at high- z and slower winds at low- z . This is in accord with our simulated redshift evolution of v_{out} , which becomes weaker at $z \leq 2$ (Fig. 12,

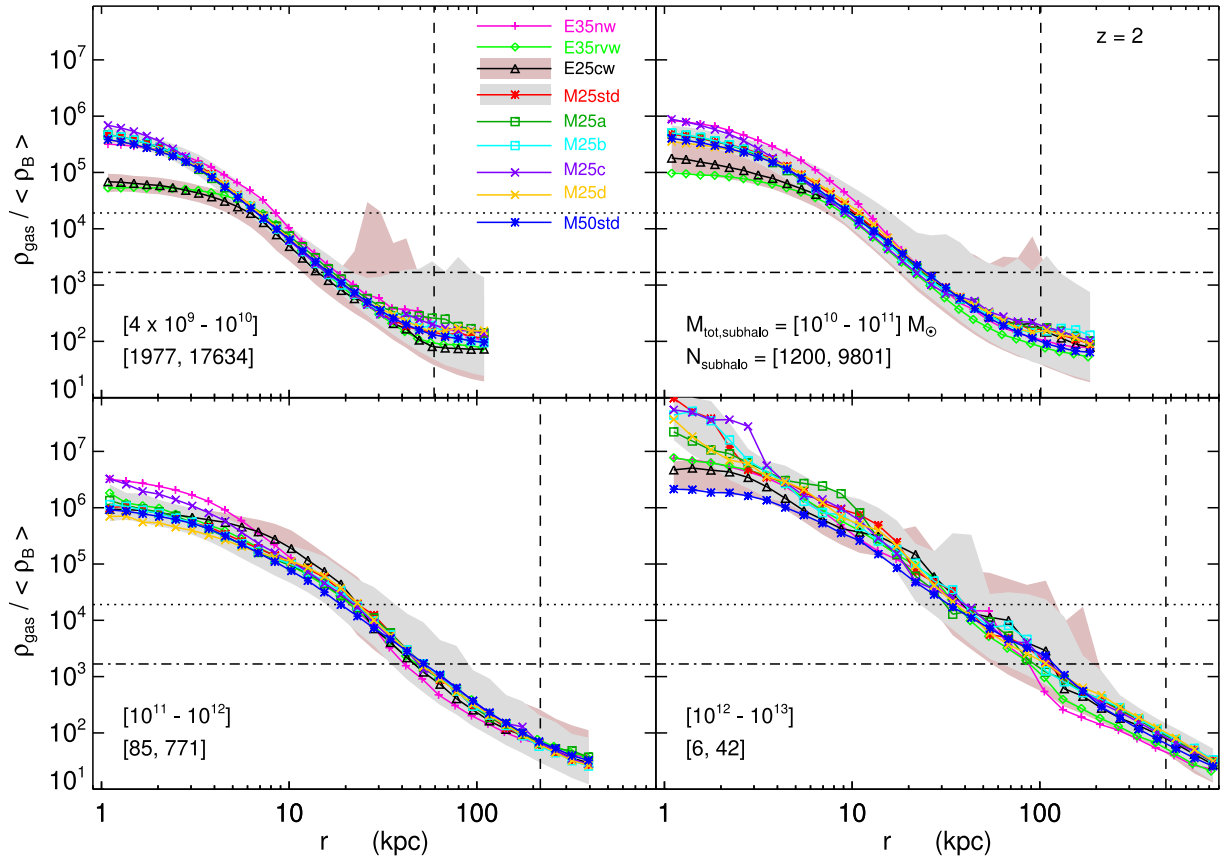


Figure 14. Radial profiles of gas overdensity around galaxy centres at $z = 2$, with the different runs labelled by the colour and plotting symbol. Overdensity is plotted as a function of galaxy radius, for four total subhalo mass ranges in the four panels: $4 \times 10^9 - 10^{10}$ (top-left), $10^{10} - 10^{11}$ (top-right), $10^{11} - 10^{12}$ (bottom-left), and $10^{12} - 10^{13}$ (bottom-right). All the subhaloes within each mass range for each run (the number mentioned in the panels) are stacked over, and the plotted curve denotes the median value in a radial bin. The shaded areas enclose the 50th percentiles above and below the median in runs *E25cw* (black curve) and *M25std* (red curve), showing the typical radial scatter. The vertical dashed line indicates the virial radius R_{200} for $M_{\text{subhalo}}/M_{\odot} = 6 \times 10^9, 3 \times 10^{10}, 3 \times 10^{11}$, and 3×10^{12} in the panels from top-left, respectively. The horizontal lines mark the SF threshold densities $n_{\text{SF}} = 0.13 \text{ cm}^{-3}$ for the effective model as dotted, and $n_{\text{SF}} = 0.01 \text{ cm}^{-3}$ for the MUPPI model as dot-dashed.

Section 4.4). This trend and the decrease of outflow detection fraction in our simulations from $z = 3$ to later epochs are in agreement with observations indicating that high- z ($z \sim 1-3$) galaxies almost ubiquitously reveal signatures of powerful winds (Veilleux et al. 2005) than those at lower z . We could not compare with the recent Illustris and EAGLE simulations, because such outflow analysis has not been presented there. Our results are consistent with the recent work by Yabe et al. (2014), who employed a simple analytic model on an observational spectroscopic sample, and found that the gas outflow rate of star-forming galaxies decreases with decreasing redshift from $z \sim 2.2$ to ~ 0 .

4.6 Radial profiles of gas properties in galaxies and their CGM at $z = 2$

The radial profiles of gas properties around galaxy centres at $z = 2$ are presented in this section, considering all the galaxies (both centrals and satellites obtained by *SUBFIND*). Each property is shown as a function of galaxy radius, or distance from the location of subhalo potential minimum. All the non-wind gas particles lying inside a distance R_{lim} from the centre are counted. The four panels denote total subhalo mass ($M_{\text{subhalo}}/M_{\odot}$) ranges: $4 \times 10^9 - 10^{10}$ (top-left) with number of subhaloes in the different simulations within the range $N_{\text{subhalo}} = 1977-17634$; $10^{10} - 10^{11}$ (top-right) having 1200-

9801 subhaloes; $10^{11} - 10^{12}$ (bottom-left) with 85-771 subhaloes; and $10^{12} - 10^{13}$ (bottom-right) with 6-42 subhaloes.

All the subhaloes within each mass range are stacked, and the plotted solid curves denote the median value in radial bins for each run. The shaded areas mark the region between 25th and 75th percentiles in runs *E25cw* (black curve) and *M25std* (red curve). It shows the typical scatter at a given radius, since galaxies do not have spherically symmetric properties in general. The vertical dashed line is the virial radius R_{200} for the following masses in the panels from top-left: $M_{\text{subhalo}}/M_{\odot} = 6 \times 10^9, 3 \times 10^{10}, 3 \times 10^{11}$, and 3×10^{12} , where the exact values are $R_{200} = 59, 101, 218$, and 470 kpc, respectively. The outer plotting radius R_{lim} is chosen to be twice the virial radius, or $R_{\text{lim}} = 2R_{200}$.

Wind particles or gas particles which have recently received a velocity kick from kinetic SN feedback and are being decoupled from hydrodynamic interactions (Sections 2.3 and 2.4) are excluded while computing the profiles.

4.6.1 Density

The gas overdensity (ratio of density to the mean baryon density) radial profiles are plotted in Fig. 14. Here the horizontal lines mark the SF threshold densities: $n_{\text{SF}} = 0.13 \text{ cm}^{-3}$ for the effective model (Section 2.3) as dotted, and $n_{\text{SF}} = 0.01 \text{ cm}^{-3}$ for the MUPPI model

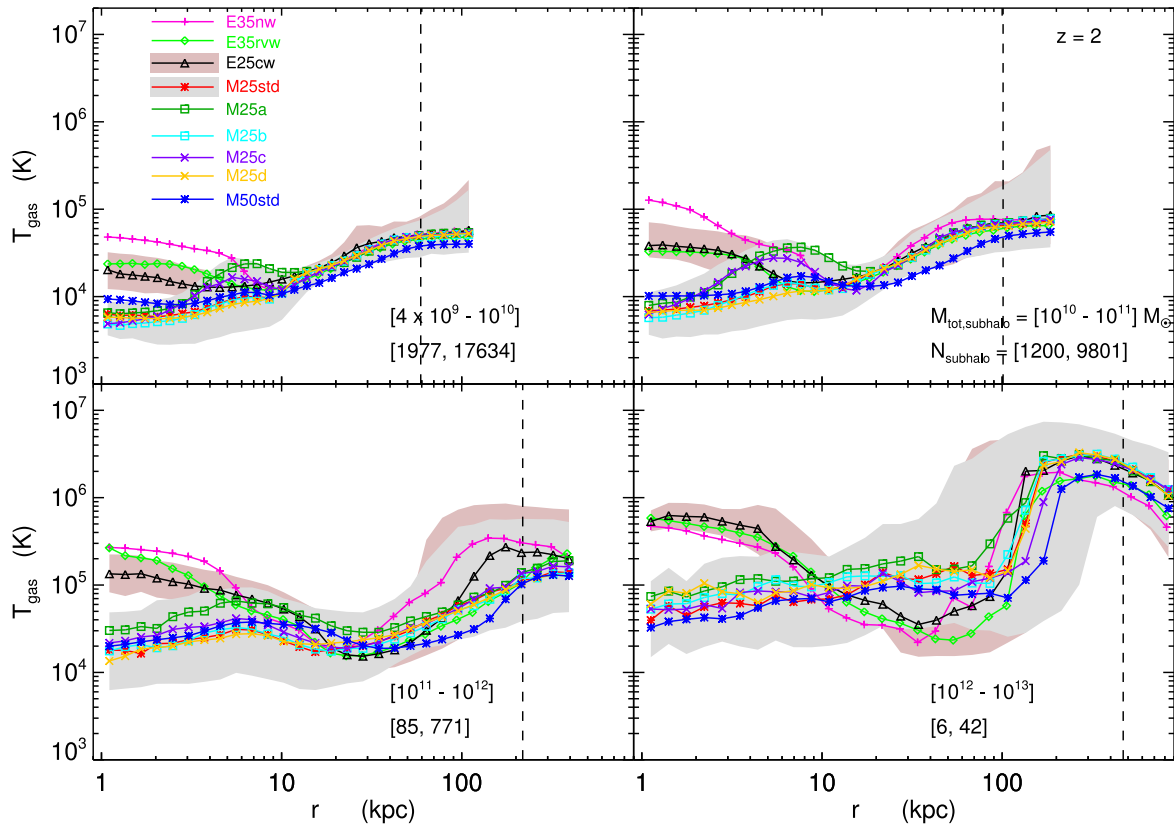


Figure 15. Radial profiles of gas temperature around galaxy centres at $z = 2$, in a format same as Fig. 14.

(Section 2.4) as dot–dashed. The gas denser than these thresholds in the respective models is forming stars. Within the approximate virial radius $r < R_{200}$, all the gas density profiles can be roughly described by two power laws with a break at an intermediate radius of ~ 10 kpc, dependent on halo mass and wind model.

The inner parts $r < 10$ kpc of the two lower subhalo mass ranges (4×10^9 – 10^{10} and 10^{10} – 10^{11} , top two panels) present notable differences: *E35rvw* and *E25cw* runs produce a lower density, by 10–30 times, than the others. The model input wind speed is independent of halo mass: constant 350 km s^{-1} in *E25cw*, and that dependent on galactocentric radius, $v_w(r)$, in *E35rvw*. Such a velocity is high enough to eject the gas away from the halo potential in low-mass galaxies, making the inner density smaller in these two runs. The central gas is not able to escape in cases *E35nw* (no-wind) which has no kinetic SN feedback, and *M25c* which has less efficient feedback, therefore, producing the highest gas density at galaxy cores than the other runs.

4.6.2 Temperature

The gas mass-weighted temperature radial profiles are presented in Fig. 15, in the same format as for density profiles. The average temperature has been used for those gas particles which are multiphase (star forming). In all the effective model runs (*E35nw*, *E35rvw*, *E25cw*), the T -profiles in the inner parts $r \leq 6$ – 30 kpc of the galaxies follow the negative-sloped density profiles (Fig. 14). This region contains dense gas forming stars at galaxy centres. The central gas undergoing SF has a warm to high temperature ($\sim 2 \times 10^4$ – 10^7 K) by construction, as a result of following the SF effective

equation of state. The MUPPI model produces a colder ($T \sim 5 \times 10^3$ – 10^5 K) galaxy core at $r \leq 4$ – 10 kpc than the effective model.

There is a change in T slope in the outer parts, at $r \geq 15$ kpc in the top two panels, and at $r \geq (80$ – $120)$ kpc in the bottom two panels; where the gas T increases with radius, because of shock heating at galaxy outskirts. The T -profiles in the two higher subhalo mass ranges (10^{11} – 10^{12} and 10^{12} – 10^{13} , bottom two panels) show a local peak at 200–300 kpc, where the infalling gas collides with that in the halo and heats, to cool before reaching the centre.

4.6.3 Metallicity

Radial profiles of gas total metallicity (Z_{gas}) are plotted in Fig. 16, showing the ratio of mass fraction of all metals in the gas to that of the Sun, $Z_{\odot} = 0.0122$. The solid curve medians and shaded area percentile values are computed considering all (both enriched and non-enriched) gas particles in radial bins. Some features of Z_{gas} are similar to the gas density profiles (Section 4.6.1), because metals are produced during SF which occurs in dense regions. At $r < (0.4$ – $0.6)R_{200}$ all the profiles show decreasing Z_{gas} going outward from centre, with varying r -dependent negative slopes.

All the MUPPI models produce relatively flatter metallicity profiles than the effective models. Note that we do not use any metal loading factor in the subresolution recipe of any model. Gas particles carry away all of the metals they contain, and pollute the CGM. The no-wind run *E35nw*, which has no kinetic SN feedback, has the highest metallicity in the inner $r < (7$ – $10)$ kpc. Wind feedback in the other runs suppresses central SF and transports some metal out, lowering the central Z_{gas} . The trend reverses in the outer $r > (7$ – $10)$ kpc: the kinetic feedback runs attain a higher Z_{gas} than

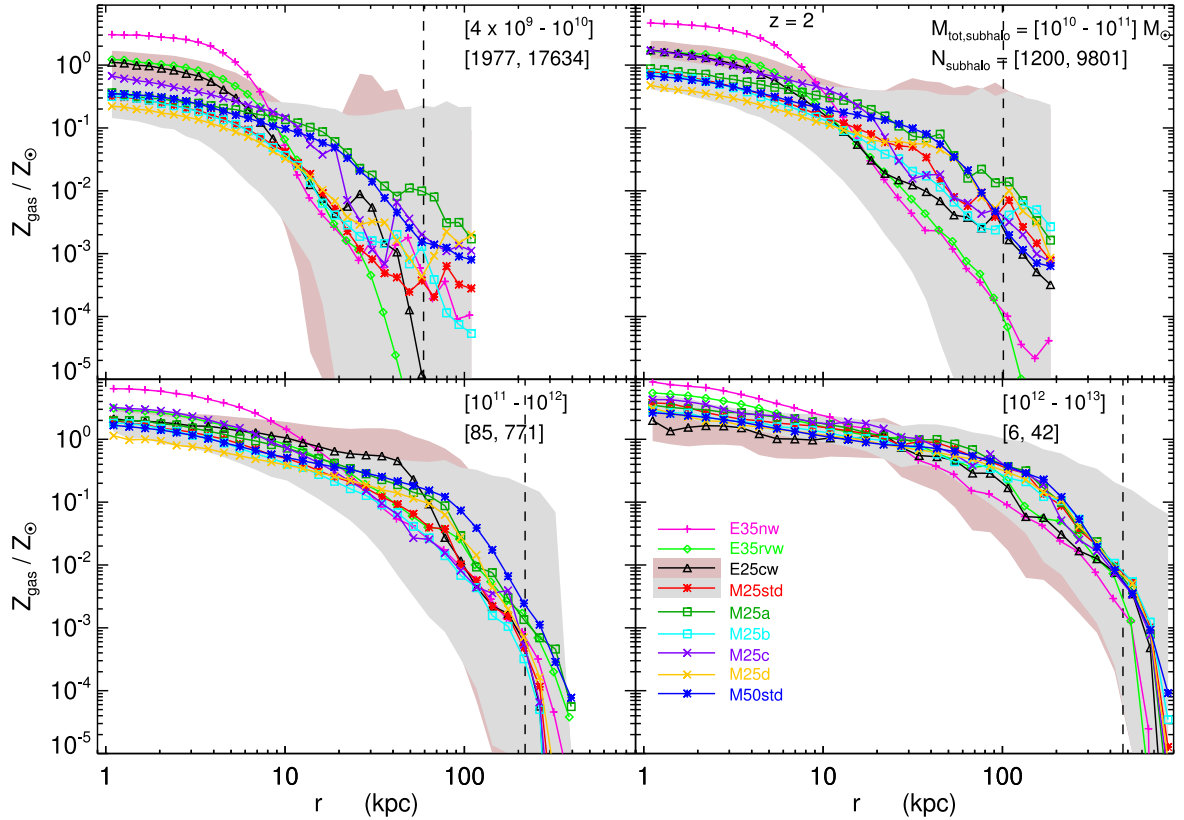


Figure 16. Radial profiles of total gas metallicity around galaxy centres at $z = 2$, in a format similar to Fig. 14. The ratio of all metal mass fraction in gas to that of the Sun ($Z_{\odot} = 0.0122$) is plotted.

E35nw, because of accumulation of metal-enriched gas expelled by wind. The differences are most prominent in the lower subhalo mass ranges ($4 \times 10^9 - 10^{10}$ and $10^{10} - 10^{11}$, top two panels), and decrease at higher masses.

We infer that MUPPI distributes metals more adequately than the effective models, which was already seen for a single galaxy in Fig. 2, fourth row.

4.6.4 Comparison of radial profiles with other works

Performing zoom-in simulations of Milky Way-mass disc galaxy formation, Hummels et al. (2013) and Marinacci et al. (2014) computed the radial profiles of diffuse CGM gas properties. Our density profiles (Section 4.6.1, Fig. 14) and metallicity profiles (Section 4.6.3, Fig. 16) are qualitatively similar to these studies. Our density profiles are also consistent to a work by Pallottini, Gallerani & Ferrara (2014). Our T -profiles (Section 4.6.2, bottom two panels of Fig. 15) present a local peak at 100–200 kpc, which is at a larger r than the peak of Hummels et al. (2013). Our Z_{gas} profiles are qualitatively consistent with observations which show breaks (changes of slope) in the radial metallicity profiles, and/or rising metallicity gradients in the outer regions of galaxies (e.g. Scarano & Lepine 2013).

5 SUMMARY AND CONCLUSION

We quantify the properties of galactic outflows and diffuse gas over $z = 1-5$ by performing cosmological hydrodynamical simulations. We explore baryonic feedback models of SF and SN feedback implemented within a modified version of the TreePM-SPH code

GADGET-3. Our novel subresolution model MUPPI (Murante et al. 2010, 2015) incorporates SF in multiphase ISM, and a direct distribution of thermal and kinetic energy from SN to the neighbouring gas, using the free parameters of feedback energy efficiency fraction and a probability. For comparison with MUPPI, we adopt the effective SF model (Springel & Hernquist 2003) with variations of kinetic SN feedback, in the energy-driven formalism. Our simulations include additional subresolution physics: metal-dependent radiative cooling and heating in the presence of photoionizing background radiation; stellar evolution and chemical enrichment.

We compare a total of nine simulations in this paper, done using the concordance Λ CDM model. We perform six new runs: five varying the SN feedback parameters of MUPPI, and one with the effective model, of a $(25 \text{ Mpc})^3$ comoving cosmological volume with 2×256^3 DM and gas particles. An additional new MUPPI run is done of a larger $(50 \text{ Mpc})^3$ box with 2×512^3 particles, to increase the galaxy statistics. Two comparison simulations are taken from Barai et al. (2013): effective SF model with no-wind and a radially varying wind case, which are $(35.56 \text{ Mpc})^3$ boxes simulated with 2×320^3 particles.

Identifying galaxies using the SUBFIND halo finder, we measure the gas outflow of each galaxy by tracking the high-speed gas particles belonging to it. Only the central galaxies having a stellar mass higher than $10^9 M_{\odot}$ are analysed. Our main findings are summarized below.

- (i) The SFRD shows that at $z < 8$ the presence of kinetic SN feedback quenches SF more than any other feature of the SF model. The simulated SFRD has a plateau maximum between $z = 2$ and 4.

(ii) Kinetic SN feedback is able to drive gas and generate high-speed outflows in galaxies of all masses reached in our simulations, $M_{\text{halo}} = (10^{10} - 10^{13}) M_{\odot}$. It also creates inflows via deceleration and later fall back of gas in the range $(1-2)R_{\text{gal}}$. Both the outflows and inflows are heated in massive galaxy haloes. We find the following trends at $z = 2$:

(a) When SN feedback is present, outflowing gas is detected in (30–97) per cent of the galaxies by number, depending on the model parameters and galaxy mass range. The number fraction of galaxies where outflow is detected increases with mass and SFR.

(b) Some outflow characteristics (listed next) exhibit positive correlations with galaxy halo, gas, and stellar masses, as well as with the SFR, which is the tightest. However, most of the cases present a large scatter.

(1) Measuring velocity of outflows by selecting gas above a fixed cut-off speed of 300 km s^{-1} , the MUPPI model generates a positive correlation of v_{out} with galaxy SFR, while the effective model shows a constant v_{out} with a large scatter.

(2) Mass outflow rate is measured by selecting gas above the escape velocity. The MUPPI model presents a stronger and relatively tighter positive correlation of \dot{M}_{out} with galaxy SFR. The effective model runs with kinetic SN feedback exhibits a weak positive correlation of \dot{M}_{out} with SFR, with a slope flatter than the MUPPI models; *E25cw* has a larger scatter, and *E35rvw* a tighter correlation. The no-wind run *E35nw* displays a scatter of \dot{M}_{out} having no relation with the SFR.

(3) The mass loading factor of the MUPPI outflows is constant with a scatter over all galaxy masses, $\eta = \dot{M}_{\text{out}}/\text{SFR} = 0.2-10$, and an average $\eta \sim 1$. The effective models generate a negative correlation of η with M_{halo} . As an exception, run *E35rvw* presents a MUPPI-like trend at lower masses ($M_{\text{halo}} < 4 \times 10^{11} M_{\odot}$): η is constant between 0.4 and 10 versus M_{halo} .

Hence the MUPPI model, *using fully local properties* of gas as input to the subresolution recipe, is able to produce galactic outflows whose velocity and mass outflow rate *correlate with global properties of the galaxy (halo mass, SFR)*. This trend is found for the first time in cosmological simulations using subresolution models. The effective model results are caused by the input fixed wind kick velocity in the energy-driven formalism.

(c) The shape of the outflows is inferred to be bipolar in ~ 95 per cent MUPPI galaxies. If outflowing gas can escape the galaxy radius, in ~ 90 per cent cases it can escape the halo gravitational potential as well at the virial radius. The mass escape at the two radii are related as $\dot{M}_{\text{out}}(R_{\text{vir}}) = 0.66 \dot{M}_{\text{out}}(R_{\text{gal}})^{0.98}$.

(d) The gas temperature radial profiles reveal that the MUPPI model produces a colder ($T \sim 5 \times 10^3 - 10^5 \text{ K}$) galaxy core at $r \leq (3-8) h^{-1} \text{ kpc}$ than the effective model.

(e) The MUPPI model generates relatively flatter gas metallicity radial profiles than the effective model.

(iii) The fraction of MUPPI galaxies exhibiting an outflow are high at all times between $z = 1$ and 5, when outflow is measured by selecting gas above the escape velocity. The outflow detection fraction decreases gradually at lower redshifts from $f_{\text{outflow}} = 0.99$ at $z = 5$ to $f_{\text{outflow}} = 0.8$ at $z \sim 1$.

The correlation between outflow velocity and SFR is positive at all the explored epochs: steeper at earlier times $z = 4-5$, and becomes flatter at later epochs. The mass loading factor is scattered within $\eta = 0.1-20$ between $z = 2$ and 5, and the average η decreases with the passage of time. Later at $z = 0.8$, η displays a negative correlation with M_{halo} at the high-mass end. The reason is the high

SFR at $z = 2-4$ driving strong outflows in galaxies, while reduced SFR at later epochs quenches the outflow driving mechanism.

(iv) Our results are overall consistent with observations of galactic winds. Galaxy population observations indicate that v_{out} increases with the SFR over $z = 0.7-2$, as we find in our simulations. Observations reveal that $z \sim 1-3$ galaxies almost ubiquitously possess powerful winds than those at lower z . This agrees with the decrease of outflow detection fraction in our simulations from $z = 3$ to later epochs.

Our analysis demonstrates the ability of the MUPPI subresolution model to generate bipolar outflows that present realistic properties. Additionally, we quantify the ability of both MUPPI and two variants of the standard energy-driven kinetic feedback model to produce significant outflows at $\sim 1/10$ of the virial radius and at the virial radius. Our study shows that in the MUPPI model the fraction of energy really used to drive these outflows is only $\sim 1/3$ or less of that used by the code.

As future work we would like to extract more observable statistics from the simulations. In particular we want to explore IGM metal enrichment by computing the Lyman α flux and simulated quasar spectra, and compare them with observations of CGM and IGM at different impact parameters from galaxies. We also plan to perform better simulations in the future: run cosmological volumes with larger box size, and include AGN feedback in our models.

ACKNOWLEDGEMENTS

We are grateful to Volker Springel for allowing us to use the GADGET-3 code. We thank Stefano Borgani, Gabriella De Lucia, David Goz, Michaela Hirschmann, Edoardo Tescari, and Luca Tornatore for useful discussions. The simulations were partly carried out at the CASPUR computing center with CPU time assigned under two standard grants. Post-processing was done on the local machine lapoderosa, and we acknowledge partial support from ‘Consorzio per la Fisica – Trieste’. PB and MV acknowledge support from the ERC Starting Grant ‘cosmoIGM’ and the INFN grant ‘INDARK’. GM and PM acknowledge support from the PRIN-INFN 2012 grant ‘The Universe in a Box: Multi-scale Simulations of Cosmic Structures’. PM acknowledges a FRA2012 grant from the University of Trieste.

REFERENCES

- Aguirre A., Hernquist L., Schaye J., Weinberg D. H., Katz N., Gardner J., 2001, *ApJ*, 560, 599
- Angles-Alcazar D., Dave R., Ozel F., Oppenheimer B. D., 2014, *ApJ*, 782, 84
- Aracil B., Petitjean P., Pichon C., Bergeron J., 2004, *A&A*, 419, 811
- Arribas S., Colina L., Bellocchi E., Maiolino R., Villar-Martin M., 2014, *A&A*, 568, A14
- Asplund M., Grevesse N., Sauval A. J., 2005, in Barnes T. G., III, Bash F. N., eds, *ASP Conf. Ser. Vol. 336, Cosmic Abundances as Records of Stellar Evolution and Nucleosynthesis*. Astron. Soc. Pac., San Francisco, p. 25
- Banerji M., Chapman S. C., Smail I., Alaghband-Zadeh S., Swinbank A. M., Dunlop J. S., Ivison R. J., Blain A. W., 2011, *MNRAS*, 418, 1071
- Barai P. et al., 2013, *MNRAS*, 430, 3213
- Baugh C. M., 2006, *Rep. Progress Phys.*, 69, 3101
- Benson A. J., 2012, *New Astron.*, 17, 175
- Bird S., Vogelsberger M., Haehnelt M., Sijacki D., Genel S., Torrey P., Springel V., Hernquist L., 2014, *MNRAS*, 445, 2313
- Bordoloi R. et al., 2014, *ApJ*, 794, 130
- Bouche N., Hohensee W., Vargas R., Kacprzak G. G., Martin C. L., Cooke J., Churchill C. W., 2012, *MNRAS*, 426, 801

- Bouwens R. J. et al., 2009, *ApJ*, 705, 936
 Bouwens R. J. et al., 2012, *ApJ*, 754, 83
 Bradshaw E. J. et al., 2013, *MNRAS*, 433, 194
 Brook C. B., Gibson B. K., Martel H., Kawata D., 2005, *ApJ*, 630, 298
 Brook C. B., Stinson G., Gibson B. K., Shen S., Maccio A. V., Obreja A., Wadsley J., Quinn T., 2014, *MNRAS*, 443, 3809
 Burbidge E. M., Burbidge G. R., Rubin V. C., 1964, *ApJ*, 140, 942
 Burke J. A., 1968, *MNRAS*, 140, 241
 Cazzoli S., Arribas S., Colina L., Piqueras-Lopez J., Bellocchi E., Emonts B., Maiolino R., 2014, *A&A*, 569, A14
 Cen R., Ostriker J. P., 2000, *ApJ*, 538, 83
 Chabrier G., 2003, *PASP*, 115, 763
 Chevalier R. A., Clegg A. W., 1985, *Nature*, 317, 44
 Choi J.-H., Nagamine K., 2011, *MNRAS*, 410, 2579
 Crighon N. H. M., Hennawi J. F., Simcoe R. A., Cooksey K. L., Murphy M. T., Fumagalli M., Prochaska J. X., Shanks T., 2015, *MNRAS*, 446, 18
 Cucciati O. et al., 2012, *A&A*, 539, A31
 Dalla Vecchia C., Schaye J., 2008, *MNRAS*, 387, 1431
 Dalla Vecchia C., Schaye J., 2012, *MNRAS*, 426, 140
 Dawson S., Spinrad H., Stern D., Dey A., van Breugel W., de Vries W., Reuland M., 2002, *ApJ*, 570, 92
 Diamond-Stanic A. M., Moustakas J., Tremonti C. A., Coil A. L., Hickox R. C., Robaina A. R., Rudnick G. H., Sell P. H., 2012, *ApJ*, 755, L26
 Dubois Y., Teyssier R., 2008, *A&A*, 477, 79
 Fabbiano G., Trinchieri G., 1984, *ApJ*, 286, 491
 Fabjan D., Borgani S., Tornatore L., Saro A., Murante G., Dolag K., 2010, *MNRAS*, 401, 1670
 Ferland G. J., Korista K. T., Verner D. A., Ferguson J. W., Kingdon J. B., Verner E. M., 1998, *PASP*, 110, 761
 Ford A. B., Dave R., Oppenheimer B. D., Katz N., Kollmeier J. A., Thompson R., Weinberg D. H., 2014, *MNRAS*, 444, 1260
 Fox A. J., Ledoux C., Petitjean P., Srianand R., 2007, *A&A*, 473, 791
 Friedli D., Benz W., 1995, *A&A*, 301, 649
 Frye B., Broadhurst T., Benitez N., 2002, *ApJ*, 568, 558
 Gauthier J.-R., Chen H.-W., 2012, *MNRAS*, 424, 1952
 Goz D., Monaco P., Murante G., Curir A., 2014, *MNRAS*, submitted
 Grimes J. P. et al., 2009, *ApJS*, 181, 272
 Haardt F., Madau P., 2001, in Neumann D. M., Van J. T. T., eds, XXXVth Rencontres de Moriond, XXIst Moriond Astrophysics Meeting, Savoie, France, p. 64
 Haas M. R., Schaye J., Booth C. M., Dalla Vecchia C., Springel V., Theuns T., Wiersma R. P. C., 2013, *MNRAS*, 435, 2931
 Heckman T. M., 2003, *Rev. Mex. Astron. Astrofis.*, 17, 47
 Hirschmann M. et al., 2013, *MNRAS*, 436, 2929
 Hummel C. B., Bryan G. L., Smith B. D., Turk M. J., 2013, *MNRAS*, 430, 1548
 Karman W., Caputi K. I., Trager S. C., Almaini O., Cirasuolo M., 2014, *A&A*, 565, A5
 Katz N., Weinberg D. H., Hernquist L., 1996, *ApJS*, 105, 19
 Kawata D., 2001, *ApJ*, 558, 598
 Kay S. T., Thomas P. A., Theuns T., 2003, *MNRAS*, 343, 608
 Komatsu E. et al., 2011, *ApJS*, 192, 18
 Kornei K. A., Shapley A. E., Martin C. L., Coil A. L., Lotz J. M., Schiminovich D., Bundy K., Noeske K. G., 2012, *ApJ*, 758, 135
 Kroupa P., Tout C. A., Gilmore G., 1993, *MNRAS*, 262, 545
 Larson R. B., Dinerstein H. L., 1975, *PASP*, 87, 911
 Lesgourgues J., Viel M., Haehnelt M. G., Massey R., 2007, *J. Cosmol. Astropart. Phys.*, 11, 008
 Lewis A., Challinor A., Lasenby A., 2000, *ApJ*, 538, 473
 Lundgren B. F. et al., 2012, *ApJ*, 760, 49
 Marinacci F., Pakmor R., Springel V., Simpson C. M., 2014, *MNRAS*, 442, 3745
 Marri S., White S. D. M., 2003, *MNRAS*, 345, 561
 Martin C. L., 1999, *ApJ*, 513, 156
 Martin C. L., 2005, *ApJ*, 621, 227
 Mathews W. G., Baker J. C., 1971, *ApJ*, 170, 241
 Monaco P., 2004, *MNRAS*, 352, 181
 Monaco P., Murante G., Borgani S., Dolag K., 2012, *MNRAS*, 421, 2485
 Mori M., Yoshii Y., Tsujimoto T., Nomoto K., 1997, *ApJ*, 478, L21
 Murante G., Monaco P., Giovalini M., Borgani S., Diaferio A., 2010, *MNRAS*, 405, 1491
 Murante G., Calabrese M., De Lucia G., Monaco P., Borgani S., Dolag K., 2012, *ApJ*, 749, L34
 Murante G., Monaco P., Borgani S., Tornatore L., Dolag K., Goz D., 2015, *MNRAS*, preprint ([arXiv:1411.3671](https://arxiv.org/abs/1411.3671))
 Murray N., Quataert E., Thompson T. A., 2005, *ApJ*, 618, 569
 Navarro J. F., White S. D. M., 1993, *MNRAS*, 265, 271
 Newman S. F. et al., 2012, *ApJ*, 752, 111
 Ohya Y., Taniguchi Y., Terlevich R., 1997, *ApJ*, 480, L9
 Okamoto T., Eke V. R., Frenk C. S., Jenkins A., 2005, *MNRAS*, 363, 1299
 Okamoto T., Frenk C. S., Jenkins A., Theuns T., 2010, *MNRAS*, 406, 208
 Oppenheimer B. D., Davé R., 2008, *MNRAS*, 387, 577
 Oppenheimer B. D., Davé R., Keres D., Fardal M., Katz N., Kollmeier J. A., Weinberg D. H., 2010, *MNRAS*, 406, 2325
 Oppenheimer B. D., Davé R., Katz N., Kollmeier J. A., Weinberg D. H., 2012, *MNRAS*, 420, 829
 Padovani P., Matteucci F., 1993, *ApJ*, 416, 26
 Pallottini A., Gallerani S., Ferrara A., 2014, *MNRAS*, 444, L105
 Perez-Gonzalez P. G. et al., 2005, *ApJ*, 630, 82
 Pettini M., Rix S. A., Steidel C. C., Adelberger K. L., Hunt M. P., Shapley A. E., 2002, *ApJ*, 569, 742
 Pinsonneault S., Martel H., Pieri M. M., 2010, *ApJ*, 725, 2087
 Piontek F., Steinmetz M., 2011, *MNRAS*, 410, 2625
 Puchwein E., Springel V., 2013, *MNRAS*, 428, 2966
 Rasera Y., Teyssier R., 2006, *A&A*, 445, 1
 Reddy N. A., Steidel C. C., 2009, *ApJ*, 692, 778
 Rodighiero G. et al., 2010, *A&A*, 515, A8
 Rubin K. H. R., Weiner B. J., Koo D. C., Martin C. L., Prochaska J. X., Coil A. L., Newman J. A., 2010, *ApJ*, 719, 1503
 Scannapieco C., Tissera P. B., White S. D. M., Springel V., 2006, *MNRAS*, 371, 1125
 Scannapieco C. et al., 2012, *MNRAS*, 423, 1726
 Scarano S., Jr, Lepine J. R. D., 2013, *MNRAS*, 428, 625
 Schaye J. et al., 2010, *MNRAS*, 402, 1536
 Schaye J. et al., 2015, *MNRAS*, 446, 521
 Schiminovich D. et al., 2005, *ApJ*, 619, L47
 Sharma M., Nath B. B., 2012, *ApJ*, 750, 55
 Shen S., Madau P., Aguirre A., Guedes J., Mayer L., Wadsley J., 2012, *ApJ*, 760, 50
 Smith B. J., Struck C., Nowak M. A., 2005, *AJ*, 129, 1350
 Sommer-Larsen J., Gotz M., Portinari L., 2003, *ApJ*, 596, 47
 Springel V., 2005, *MNRAS*, 364, 1105
 Springel V., Hernquist L., 2003, *MNRAS*, 339, 289
 Steidel C. C., Erb D. K., Shapley A. E., Pettini M., Reddy N., Bogosavljevic M., Rudie G. C., Rakic O., 2010, *ApJ*, 717, 289
 Steidel C. C., Bogosavljevic M., Shapley A. E., Kollmeier J. A., Reddy N. A., Erb D. K., Pettini M., 2011, *ApJ*, 736, 160
 Stinson G., Seth A., Katz N., Wadsley J., Governato F., Quinn T., 2006, *MNRAS*, 373, 1074
 Stinson G. S., Dalcanton J. J., Quinn T., Kaufmann T., Wadsley J., 2007, *ApJ*, 667, 170
 Sutherland R. S., Dopita M. A., 1993, *ApJS*, 88, 253
 Tang Y., Giallisco M., Guo Y., Kurk J., 2014, *ApJ*, 793, 92
 Tescari E., Viel M., Tornatore L., Borgani S., 2009, *MNRAS*, 397, 411
 Tescari E., Viel M., D'Odorico V., Cristiani S., Calura F., Borgani S., Tornatore L., 2011, *MNRAS*, 411, 826
 Tescari E., Katsianis A., Wyithe J. S. B., Dolag K., Tornatore L., Barai P., Viel M., Borgani S., 2014, *MNRAS*, 438, 3490
 Thacker R. J., Couchman H. M. P., 2000, *ApJ*, 545, 728
 Theuns T., Viel M., Kay S., Schaye J., Carswell R. F., Tzanavaris P., 2002, *ApJ*, 578, L5
 Thielemann F.-K. et al., 2003, *Nucl. Phys. A*, 718, 139
 Thompson T. A., Fabian A. C., Quataert E., Murray N., 2014, preprint ([arXiv:1406.5206](https://arxiv.org/abs/1406.5206))

- Tornatore L., Borgani S., Matteucci F., Recchi S., Tozzi P., 2004, MNRAS, 349, L19
- Tornatore L., Borgani S., Dolag K., Matteucci F., 2007, MNRAS, 382, 1050
- Vader J. P., 1986, ApJ, 305, 669
- van den Hoek L. B., Groenewegen M. A. T., 1997, A&AS, 123, 305
- van der Burg R. F. J., Hildebrandt H., Erben T., 2010, A&A, 523, A74
- van de Voort F., Schaye J., 2012, MNRAS, 423, 2991
- Vazza F., Gheller C., Bruggen M., 2014, MNRAS, 439, 2662
- Veilleux S., Cecil G., Bland-Hawthorn J., 2005, ARA&A, 43, 769
- Vikhlinin A. et al., 2009, ApJ, 692, 1060
- Vogelsberger M. et al., 2014, MNRAS, 444, 1518
- von Glasow W., Krause M. G. H., Sommer-Larsen J., Burkert A., 2013, MNRAS, 434, 1151
- Weil M. L., Eke V. R., Efstathiou G., 1998, MNRAS, 300, 773
- Weiner B. J. et al., 2009, ApJ, 692, 187
- Wiersma R. P. C., Schaye J., Smith B. D., 2009, MNRAS, 393, 99
- Wilman R. J., Gerssen J., Bower R. G., Morris S. L., Bacon R., de Zeeuw P. T., Davies R. L., 2005, Nature, 436, 227
- Woosley S. E., Weaver T. A., 1995, ApJS, 101, 181
- Yabe K., Ohta K., Akiyama M., Iwamuro F., Tamura N., Yuma S., Dalton G., Lewis I., 2014, ApJ, preprint ([arXiv:1410.7147](https://arxiv.org/abs/1410.7147))

This paper has been typeset from a $\text{\TeX}/\text{\LaTeX}$ file prepared by the author.